Alma Mater Studiorum · Università di Bologna

Scuola di Scienze

Corso di Laurea Magistrale in Fisica

The Atmospheric Stable Boundary Layer: Data Analysis and Comparison with Similarity Theories

Relatore:

Prof. Francesco Tampieri

Presentata da:

Matteo Michelotti

Sessione II

Anno Accademico 2012/2013

Contents

List of Figures

Sommario

L'obiettivo di questa dissertazione è quello di studiare la struttura e il comportamento dello Strato Limite Atmosferico, in condizioni stabili. Questo tipo di strato limite non è ancora completemente compreso appieno, anche se è molto importante per molti utilizzi pratici, che vanno dalla modellizzazione previsionale, alla dispersione di agenti inquinanti in atmosfera.

Abbiamo analizzato dati provenienti dall'esperimento SABLES98 (Stable Atmospheric Boundary Layer Experiment in Spain, 1998), e comparato il comportamento di questi dati utilizzando le funzioni di similarità di Monin-Obukhov, per la velocità del vento e la temperatura potenziale.

Analizzando i profili verticali di diverse variabili, in particolare i flussi di calore e di quantità di moto, abbiamo identificato due strutture contrastanti che descrivono due differenti stati dello strato limite stabile, uno *tradizionale* ed uno *sottosopra*.

Siamo stati in grado di determinare le principali caratteristiche di questi due stati in termini di profili verticali di temperatura potenziale, della velocità del vento, dell'energia cinetica e dei flussi turbolenti, studiando le serie temporali e le strutture verticali dell'atmosfera per due notti dell'esperimento, prese come casi studio.

Abbiamo inoltre sviluppato una classificazione originale dello strato limite stabile, per separare l'influenza dei fenomeni a mesoscala dalle caratteristiche puramente turbolente, usando come parametri la velocità del vento e il numero di Richardson di gradiente.

Abbiamo quindi confrontato queste due formulazioni, usando i dati provenienti dal dataset SABLES98, verificando la loro validità con diverse variabili (velocità del vento, temperatura potenziale e loro differenze a diverse quote) e con diversi parametri di stabilità (ζ oppure R_g).

Nonostante la diversa base fisica delle due formulazioni, è stato possibile identificare dei comportamenti comuni, specialmente in condizioni di bassa stabilità.

Abstract

The objective of this dissertation is to study the structure and behavior of the Atmospheric Boundary Layer (ABL) in stable conditions. This type of boundary layer is not completely well understood yet, although it is very important for many practical uses, from forecast modeling to atmospheric dispersion of pollutants.

We analyzed data from the SABLES98 experiment (Stable Atmospheric Boundary Layer Experiment in Spain, 1998), and compared the behaviour of this data using Monin-Obukhov's similarity functions for wind speed and potential temperature.

Analyzing the vertical profiles of various variables, in particular the thermal and momentum fluxes, we identified two main contrasting structures describing two different states of the SBL, a *traditional* and an *upside-down* boundary layer.

We were able to determine the main features of these two states of the boundary layer in terms of vertical profiles of potential temperature and wind speed, turbulent kinetic energy and fluxes, studying the time series and vertical structure of the atmosphere for two separate nights in the dataset, taken as case studies.

We also developed an original classification of the SBL, in order to separate the influence of mesoscale phenomena from turbulent behavior, using as parameters the wind speed and the gradient Richardson number.

We then compared these two formulations, using the SABLES98 dataset, verifying their validity for different variables (wind speed and potential temperature, and their difference, at different heights) and with different stability parameters (ζ or R_g).

Despite these two classifications having completely different physical origins, we were able to find some common behavior, in particular under weak stability conditions.

Chapter 1

Introduction

1.1 The Atmosphere

The atmosphere is the thin gaseous layer that surrounds the entirety of the planet, and it is retained by the gravitational attraction of the Earth itself. Due to gravity, the atmosphere becomes thinner with increasing altitude without an abrupt end at any given height. Therefore, it is not possible to find a definite boundary between the atmosphere and outer space. However, such a separation is often considered at around 100 km, the height at which the air becomes too thin to allow aeronautical flight. This altitude is called "Karman line", and it was named after Theodore von Karman (1881-1963), a Hungarian-American engineer and physicist who was active primarily in the field of aeronautics and astronautics.

The atmospheric stratification describes the structure of the atmosphere, dividing it into distinct layers, each with specific characteristics such as temperature or composition. The main parameter that defines the separation between the different layers is the temperature, mainly because the temperature gradient is a fundamental parameter to define the stability of the atmosphere. Within this classification one can identify four fundamental layers, called (from the lowest to the highest) *Troposphere*, *Stratosphere*, *Mesosphere* and *Thermosphere*, divided by relatively thin layers where the temperature is almost constant with height called pauses.

1.1.1 Troposphere

The troposphere is the lowest portion of the Earth's atmosphere. It contains approximately 80% of the atmosphere's mass and 99% of its water vapor and aerosols. The average depth of the troposphere is between 10-15 km, depending strongly on latitude and time of year. It is characterized by decreasing temperature with height, with an average temperature lapse rate of about 6.5 K/km and an elevated ability of vertical mixing between the layers closer to the ground and the ones above.

It is possible to divide the troposphere into two different layers based on its interaction with the surface: the lower level is called *planetary boundary layer*, while the level on top is called free atmosphere, but we'll discuss more about this particular aspect later in the essay.

1.1.2 Stratosphere

The stratosphere is the layer above the so-called tropopause, a thin layer that separates the troposphere and stratosphere. The pauses are always present between layers, and are defined by the *WMO* as those layers at which the lapse rate decreases to 2 K/km or less, provided that the average lapse rate between this level and all higher levels within 2 km does not exceed 2 K/km.

Within the stratosphere, vertical mixing is strongly inhibited by the increase of temperature with height caused by the strong absorption of solar radiation in the ultraviolet region of the spectrum from the ozone, particularly abundant in this layer. In addition to the high concentration of ozone, there is a very low concentration of water vapor. For this reason, cloud processes play a much more limited role in removing particles injected by volcanic eruptions and human activities than they do in the troposphere, so residence times of particles tend to be correspondingly longer in the stratosphere. The temperature maximum caused by the ozone activity is at about 50 km, the height that defines the stratopause, underneath which is concentrated approximately 99.9% of the mass of the atmosphere.

1.1.3 Mesosphere

In the mesosphere, the temperature decreases with height once again, a process started because the ozone chemical reactions are much less efficient here, since density has lowered consistently, and their absorption of radiation is not enough to counterbalance the emission to space. This in turn generates moderate vertical instability and mixing, which could cause the formation of thin cloud layers called noctilucent clouds.

1.1.4 Thermosphere

Above the mesopause, at about 80 km of height, the temperature rises again due to the absorption of solar radiation in association with the dissociation of diatomic nitrogen and oxygen molecules and the stripping of electrons from atoms, processes referred to as photodissociation and photoionization. Temperature in the Earth's outer thermosphere varies widely in response to variations in the emission of ultraviolet and x-ray radiation from the sun's outer atmosphere.

Of all these different layers, the one where the greatest number of meteorological phenomena reside, and so the most interesting for what concerns life on the surface of the Earth, is the troposphere. In particular, in this essay we will focus our attention on the first and lower part of the troposphere, because of its peculiar behavior yet to be fully explored and understood, the *planetary boundary layer*.

1.2 Planetary Boundary Layer

As we previously stated, the lower portion of the troposphere is the so-called *planetary boundary layer* (PBL) or *atmospheric boundary layer* (ABL), which is a strongly turbulent layer immediately affected by the dynamic, thermal and other interactions with the underlying land/water surface. Human life and activities develop mainly in this physical space, and in this atmospheric portion is concentrated the majority of the emissions of pollutants, both natural and anthropogenic.

The thickness of the boundary layer is quite variable in space and time, and can range from tens of meters (mainly in the nocturnal hours) to a few kilometers (when the insulation of the surface is maximum). Normally this temporal variability has a pronounced diurnal cycle, which shows how the PBL could be considered as a huge thermal machine that transforms available solar energy in motion of the air masses [Stull, 1988]. It is possible to see a schematic evolution of the boundary layer in the following picture (Fig. 1.1).

Turbulence and static stability act together to tightly insert a strong stable layer (called a *capping inversion*) between the boundary layer below and the rest of the troposphere above (called the *free atmosphere*). This stable layer traps turbulence, pollutants, and moisture below it and prevents most of the surface friction from being felt by the free atmosphere.

The boundary layer is said to be *unstable* whenever the surface is warmer than the air, such as during a sunny day with light winds over land, or when cold air is advected over a warmer water surface. This boundary layer is in a state of *free convection*, with vigorous thermal updrafts and downdrafts, which is the reason why it's called *Convective Boundary Layer* (CBL). In this layer, turbulence is generated by the heat flux at the surface, causing the virtual temperature profile to be unstable (over-adiabatic) in the vicinity of the surface, and almost adiabatic in the middle region, well mixed. Similarly, the gradient of the wind (*wind shear*) is weak in the middle portion and can be greater at the lower or higher layers, where it can cause instabilities and turbulence.

The boundary layer is said to be stable (*Stable Boundary Layer* - SBL)

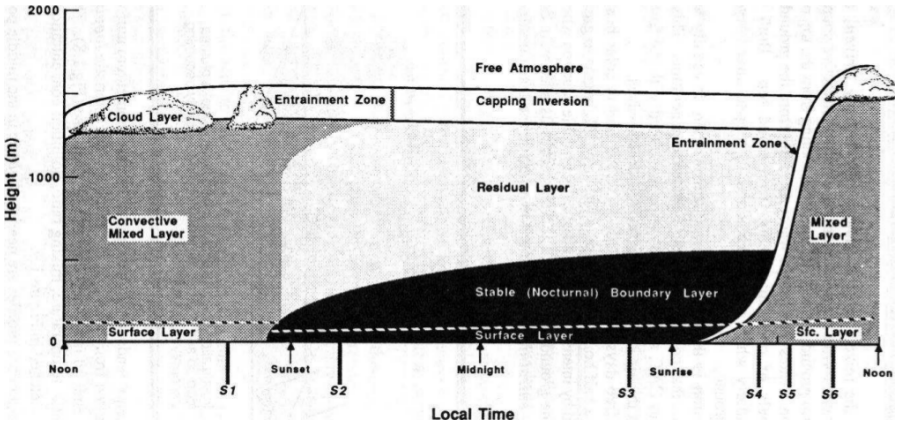

Figure 1.1: *Idealized time evolution of the atmospheric boundary layer [Stull, 1988].*

when the surface is colder than the air, such as during a clear night over land, or when warm air is advected over colder water. The turbulence is generated by the wind shear, and it is attenuated by the stable stratification. In strong stable conditions, and in absence of shear, the turbulence can disappear or act intermittently. Usually the wind presents great vertical velocity gradients that at lower levels can create local maximum of velocity (called *Low Level Jet* - LLJ), which determine the partial decoupling between the atmosphere and the ground (Banta et al. [2007], Banta [2008]).

The boundary layer approaches neutrality when the thermal exchanges between air and surface are minimal. This can be accomplished when the air masses are in thermal equilibrium with the surface (for example over the sea), or when the exchange due to turbulence is elevated.

Turbulent communication between the surface and the air is quite rapid, allowing the air to quickly take on characteristics of the underlying surface. In fact, one definition of the boundary layer is that portion of the lower atmosphere that feels the effects of the underlying surface within about 30 minutes or less.

"*Turbulence is inspiringly complex, consisting of a superposition of swirls called eddies that interact non-linearly to create quasi-random, chaotic motions. An infinite number of equations is required to fully describe these motions. Hence, a complete solution has not been found.*" -Wallace and Hobbs [2006]

1.3 Static Stability

Consider a layer of the atmosphere in which the actual temperature lapse rate is Γ with temperature T' and density ρ'. If a parcel of unsaturated air with temperature T and density ρ is displaced across this layer without any exchange of mass or energy (adiabatic motion, defined by a temperature lapse rate $\Gamma_d = 9.8K/km$), and supposing that the movement is slow enough to guarantee the pressure of the parcel adjusts immediately to the pressure of the environment, the parcel will find itself in an environment with a different temperature, higher or lower depending on the lapse rate Γ.

Therefore, on this parcel acts a force per unit volume calculated by the well-known Archimedes principle, that is:

$$F = g \cdot (\rho - \rho') \rightarrow \frac{d^2 z}{dt^2} = g \cdot \left(\frac{\rho - \rho'}{\rho} \right) \tag{1.1}$$

where z is the height of the air parcel. Using the gas equation ($P = R_d \rho T$), the densities of the air parcel and the ambient air are inversely proportional to their temperatures, leading to:

$$\frac{d^2 z}{dt^2} = g \cdot \left(\frac{T' - T}{T} \right) = g \cdot \left(\frac{\theta' - \theta}{\theta} \right) \tag{1.2}$$

where, for the last passage, we used the definition of potential temperature and that the pressure of the environment and the parcel are constantly equal.

Let $z = z_0$ be the equilibrium level of the air parcel and $z' = z - z_0$ be the vertical displacement of the air parcel from its equilibrium level, and let T_0 be the environmental air temperature at $z = z_0$. If the air parcel is adiabatically lifted through a distance z' from its equilibrium level, its temperature will then be $T' = T_0 - \Gamma_d \cdot z'$, therefore $T' - T = -(\Gamma_d - \Gamma) z'$. Substituting this last expression into the equation of the motion, we obtain:

$$\frac{d^2 z'}{dt^2} = -\frac{g}{T} \left(\Gamma_d - \Gamma \right) z' \tag{1.3}$$

which could be rewritten using the definition of the Brunt-Vaisala frequency $N^2 = \frac{g}{T}(\Gamma_d - \Gamma)$ as a second order differential equation in the form of:

$$\frac{d^2 z'}{dt^2} = -N^2 z' \tag{1.4}$$

This equation can be solved depending on the sign of the constant $-N^2$, which depends only over the sign of the difference between the environment and the adiabatic lapse rates Γ_d and Γ.

- If $\Gamma_d > \Gamma$, or in terms of potential temperature if $\frac{d\theta}{dz} > 0$, the Brunt-Vaisala frequency is positive, the differential equation solution is a buoyancy oscillation, which means the PBL is statically *stable*.

- If $\Gamma_d < \Gamma$, or in terms of potential temperature if $\frac{d\theta}{dz} < 0$, the Brunt-Vaisala frequency is negative, the differential equation leads to an *unstable* situation where the solution is diverging per every displacement of the parcel of air.

- If $\Gamma_d = \Gamma$, or in terms of potential temperature if $\frac{d\theta}{dz} = 0$, the Brunt-Vaisala frequency is also zero, leading to the trivial solution of uniform motion after the parcel displacement (condition of *static neutrality*).

Because these concepts of the stability of the atmosphere are not sufficient to portray the behavior of the planetary boundary layer, we need to describe another very important aspect that represents the PBL: the atmospheric turbulence.

1.4 Turbulence and Turbulent Motion

The motion of a viscous fluid can be classified in two different ways: *laminar* and *turbulent*.

A laminar motion is ordinate, where adjacent layers of fluid flow on top of each other with a very small mixing and with an exchange of properties merely at molecular scale. In a laminar motion, the fields associated to the fluid (such as temperature, velocity and concentration) are highly regular and can vary only slowly in time and space. An interesting aspect of a laminar motion is its behavior in the proximity of a rigid boundary due to its intrinsic viscosity. In fact, the particles of the fluid stick to the solid surface with which they are in direct contact, causing no relative motion between the latter and the fluid, an effect called *"no-slip condition"*.

The analysis of the velocity profile of such a fluid shows that this condition illustrates that the velocity is null by the surface and raises until it reaches an equilibrium value far away from said surface. Therefore there can be found a layer with a depth of h where the motion is disturbed by the surface called *boundary layer*.

This is indeed an ideal case that can however be recreated with highly viscous fluids in slow motion over a very smooth surface. In reality, when the surface is rough, the velocity greater and the viscosity lower, the motion shows a dramatically different face, with many irregularities both in space and time. In this frame of reference, the most important parameters that characterize the fluid are the velocity U, the depth of the boundary layer h and the kinematic viscosity ν.

Reynolds introduced a proxy to determine the different flow regimes using precisely these parameters, called the *Reynolds number*, that gives a measure of the ratio of the inertial forces to the viscous forces of a given flow:

$$Re = \frac{Uh}{\nu} \tag{1.5}$$

Varying the values of the parameters, namely varying the value of the Reynolds number, one can recognize three different regimes (Sozzi et al. [2002]):

- for low Reynolds numbers (of the order of $10^1 - 10^2$), the motion of the fluid is very regular, showing a laminar behavior.

- Above this critical value, which can vary depending over many factors like the roughness of the surface or its geometry, but always of the order of 10^3, the fluid starts showing the first signs of turbulence, with two-dimensional instabilities that can become three-dimensional with increasing Reynolds numbers.

- At high Reynolds numbers, these three-dimensional random disturbances rise in number, frequency, intensity; they mix together and break apart, until they affect all the fluid in the boundary layer. The motion of the fluid is now very different from its original state: a motion that resembles a laminar flow can be still identified, but with a superimposed component of more or less intense disturbances, that can be described as quasi-random, chaotic, or *turbulent*.

It is quite challenging trying to give a specific definition of turbulence, however, it is possible to define it through some of its main characteristics and properties (Sozzi et al. [2002]):

1. **Irregularity**: The most evident feature in a turbulent fluid its the extreme irregularity in its main variable's fields. These irregularities resemble those of a stochastic phenomena, suggesting a statistical approach to describe it.

2. **High Reynolds numbers**: Turbulence is generated only at high Reynolds numbers, meaning that the inertial forces (which act towards the destabilization of the motion of the fluid) prevail over the viscous forces (which instead regulate the motion).

3. **Diffusivity**: The irregularities of a turbulent fluid determine a quick mixing of the different portions that compose the fluid, acting to increase the transfer of mass, momentum, and heat.

4. **Dissipation**: the viscous forces generate deformation work on the fluid, which increase the internal energy of the latter at the expense of its kinetic energy. Therefore, in order to maintain a turbulent motion, a constant input of energy is required.

5. **Continuity**: The turbulence is not a microscopic phenomena, but macroscopic, therefore it is governed by the laws of fluid mechanics. This statement might seem to conflict with the first one listed, however, it does not. It is possible to create a theoretical apparatus using the laws of fluid mechanics, nevertheless the presence of non-linear effects within it can explain the chaotic behavior of the turbulence and show that this construct is not able to produce a complete model.

For what concerns the planetary boundary layer, using the typical values for vertical extension (of the order of 10^3 m) and wind speed (about $5 - 10m/s$), the approximate value of the Reynolds number is around $10^8 - 10^9$, implying a very turbulent motion. This aspect it's noticeable in field observations, like in Fig. 1.2, which represents the temporal evolution of the wind components. The extreme irregularity that can be seen is the fingerprint of the turbulence itself. Bearing in mind the idea of a stochastic description, Reynolds advanced the hypothesis of separating the motion in two components: an *average* motion, essentially deterministic, and a *turbulent* set of fluctuations of stochastic nature.

Following Reynolds' hypothesis, a generic variable U in a determined point in space and time could be expressed by the following relation:

$$U(\overline{x}, t) = \overline{U}(\overline{x}, t) + u'(\overline{x}, t) \tag{1.6}$$

where $\overline{U}$ is the average value, $\overline{x}$ is a generic point is space, and u' is the turbulent fluctuation. Reynolds also defined a set of conditions that this variables have to follow:

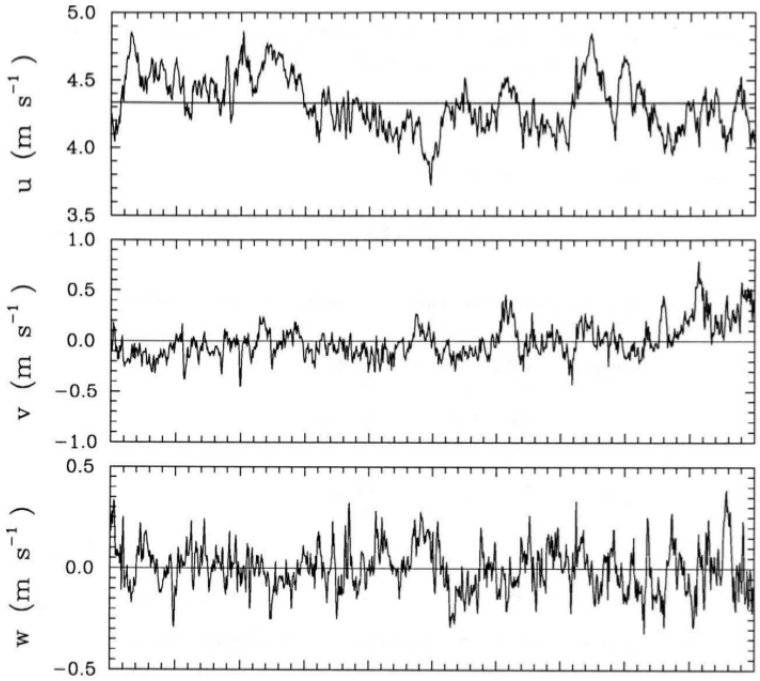

Figure 1.2: *Time series of the three components of the wind speed in the surface layer, from Trombetti and Tagliazucca [1994].*

$$\overline{U+V} = \overline{U} + \overline{V}, \tag{1.7a}$$

$$\overline{aU} = a\overline{U}, \qquad a = const. \tag{1.7b}$$

$$\overline{a} = a, \tag{1.7c}$$

$$\overline{\frac{\partial U}{\partial x_i}} = \frac{\partial \overline{U}}{\partial x_i}, \qquad x_i = \{x, y, z, t\} \tag{1.7d}$$

$$\overline{\overline{U} \cdot V} = \overline{U} \cdot \overline{V} \tag{1.7e}$$

From these rules, and remembering that the mean value of a fluctuation is always zero, the mean value of the product of two variables A and B can be easily determined:

$$\begin{aligned}
\overline{(A \cdot B)} &= \overline{(\overline{A} + a') \cdot (\overline{B} + b')} \\
&= \overline{(\overline{A} \cdot \overline{B} + \overline{A} \cdot b' + a' \cdot \overline{B} + a' \cdot b')} \\
&= \overline{(\overline{A} \cdot \overline{B})} + \overline{(\overline{A} \cdot b')} + \overline{(a' \cdot \overline{B})} + \overline{(a' \cdot b')} \\
&= (\overline{A} \cdot \overline{B}) + (\overline{A} \cdot \overline{b'}) + (\overline{a'} \cdot \overline{B}) + \overline{(a' \cdot b')} \\
&= \overline{A} \cdot \overline{B} + \overline{a' \cdot b'}
\end{aligned} \tag{1.8}$$

In reality, what we usually measure is not the continuous time evolution of a meteorological variable U, but only a discretization of the real behavior through a set of points separated by a time interval Δt, depending on the sampling frequency. So, the time average between two instants t_1 and $t_2 = t_1 + N \cdot \Delta t$ is given by

$$\overline{U} = \frac{1}{N} \sum_{i=1}^{N} U_i \tag{1.9}$$

that represents a good estimator of the true average value if the number of samples is sufficiently elevated. In order to measure the dispersion of the data from the average, we need to introduce the variance, and a good estimator is going to be:

$$\sigma_u^2 = \frac{1}{N-1} \sum_{i=1}^{N} (U_i - \overline{U})^2 \tag{1.10}$$

that can be re-written using Eq. 1.6, becoming:

$$\sigma_u^2 = \frac{1}{N-1} \sum_{i=1}^{N} (u')^2 = \overline{u'^2} \tag{1.11}$$

It is also very useful to know how much two meteorological quantities A and B that evolve in time are correlated to each other. One of the best tools to determine this is the covariance, defined by:

$$Cov(A, B) = \frac{1}{N} \sum_{i=1}^{N} \left[\left(A_i - \overline{A} \right) \cdot \left(B_i - \overline{B} \right) \right] = \frac{1}{N} \sum_{i=1}^{N} a'b' = \overline{a'b'} \tag{1.12}$$

This statistical approach is very powerful because it allows us to relate the velocity variances to the kinetic energy associated with the motion of the turbulence. Similarly the covariance is a measure of the flux caused by these motions.

1.4.1 Turbulent Kinetic Energy

The classical formulation for the specific kinetic energy (per unit mass) of a moving object with mass m and velocity v is:

$$\frac{KE}{m} = \frac{1}{2}v^2 \tag{1.13}$$

By extension, we can define the mean kinetic energy of an air parcel using the three components of its velocity, and using Reynolds' hypothesis (Eq. 1.6) we obtain:

$$\begin{aligned} \frac{KE}{m} &= \frac{1}{2}\overline{(u^2 + v^2 + w^2)} \\ &= \frac{1}{2}\left[\left(\overline{u}^2 + \overline{v}^2 + \overline{w}^2\right) + \left(\overline{u'^2} + \overline{v'^2} + \overline{w'^2}\right)\right] \\ &= MKE + TKE \end{aligned} \tag{1.14}$$

where we defined the first term of the sum *Mean Kinetic Energy* (MKE), which describes the kinetic energy of the mean flow, and the second term is the *Turbulent Kinetic Energy* (TKE), that is the kinetic energy generated by the turbulence itself. With this formulation, we see that for a laminar flow, which contains no microscale motions, the TKE will be zero.

1.4.2 Turbulent Fluxes

The motion of the air masses in the planetary boundary layer implies that in a generic point $P(x, y, z, t)$ will develop fluxes of momentum, heat and other variables. It is possible to see that these fluxes are related to the covariances of some of the variables of interest.

For example, in the case of the heat, the flux in the direction $\hat{\imath}$ is:

$$Q_i = \rho C_p \cdot T \cdot u_i$$

where ρ is the air density, C_p is the specific heat at constant pressure, T the temperature and $u_i = (u, v, w)$ the wind speed in the î direction . This quantity is going to have the same stochastic behavior of the three wind components and the temperature, so we need to calculate the mean flux over a time interval τ:

$$\overline{Q_i} = \frac{\rho C_p}{\tau} \int_{t_1}^{t_1+\tau} u_i(t) \cdot T(t) dt = \rho C_p \cdot \overline{u_i(t) \cdot T(t)} \tag{1.15}$$

Using Reynolds' hypothesis and in particular Eq. 1.8, we can find that the mean flux is composed by two parts:

$$\overline{Q_i} = \rho C_p \overline{u_i} \cdot \overline{T} + \rho C_p \overline{u_i' \cdot T'} = \overline{Q_{i\_kin}} + \overline{Q_{i\_turb}} \tag{1.16}$$

where we defined $\overline{Q_{i\_kin}}$ as the *kinematic heat flux* due to the transport of heat done by the mean motion of the air masses and the $\overline{Q_{i\_turb}}$ as the *turbulent heat flux* caused by the turbulent motions. It is worth noting that, even in absence of a mean motion of the fluid, the sole turbulence is able to transfer heat.

Similar considerations could be done for the flux of momentum, made slightly more complicated by the fact that the momentum is a vectorial variable, not scalar as is the temperature. In fact, it can be easily demonstrated that the *mean flux of momentum* is a 3x3 tensor, which can be expressed like this:

$$\overline{F_p} = \rho \cdot \begin{vmatrix} \overline{U} \cdot \overline{U} & \overline{V} \cdot \overline{U} & \overline{W} \cdot \overline{U} \\ \overline{U} \cdot \overline{V} & \overline{V} \cdot \overline{V} & \overline{W} \cdot \overline{V} \\ \overline{U} \cdot \overline{W} & \overline{V} \cdot \overline{W} & \overline{W} \cdot \overline{W} \end{vmatrix} + \rho \cdot \begin{vmatrix} \overline{u'u'} & \overline{v'u'} & \overline{w'u'} \\ \overline{u'v'} & \overline{v'v'} & \overline{w'v'} \\ \overline{u'w'} & \overline{v'w'} & \overline{w'w'} \end{vmatrix} \tag{1.17}$$

As for the mean heat flux in Eq. 1.16, we can recognize that the first addend represent the *Kinematic Flux of Momentum*, while the second is the *Turbulent Flux*. We can now see how covariances can be interpreted as fluxes

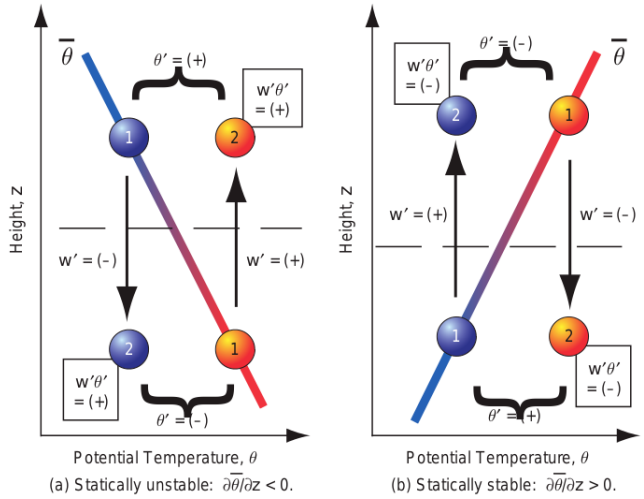

Figure 1.3: *Illustration of how to anticipate the sign of turbulent heat flux for small-eddy (local) vertical mixing across a region with a linear gradient in the mean potential temperature (from Wallace and Hobbs [2006]).*

using the following concept. Consider a portion of the atmosphere with a constant gradient of potential temperature as sketched in Fig. 1.3. Consider an idealized eddy circulation consisting of an updraft portion that moves an air parcel from the bottom to the top of the layer and a compensating downdraft that moves a different air parcel downward. The moving parcels carry with them air from their starting points, which preserves its potential temperature as it moves. We can see that as the parcels move up ($w' > 0$) or down ($w' < 0$), depending on the vertical gradient of potential temperature, they will end up in a portion of atmosphere hotter ($\theta' < 0$) or colder ($\theta' > 0$), which determines the sign of the product $w' \cdot \theta'$. Thus, positive $\overline{w'\theta'}$ covariance is associated with warm air moving up and/or cold air moving down, namely a *positive* heat flux, and negative covariance is associated with cold air moving up and/or warm air moving down, namely *negative* heat flux.

The same considerations can be done for every component of the flux of momentum (e.g. $\overline{u'w'}$). In a normal situation, where the wind increases with height, a positive vertical displacement of the parcel ($w' > 0$) will cause a negative difference in the horizontal velocity ($u' < 0$), and vice versa, therefore the horizontal turbulent flux of momentum is always negative.

1.5 Equations and Closure Problem

1.5.1 Equations for the istantaneous quantities

Theoretically, in order to describe a mathematical model of the planetary boundary layer, it is reasonable to find the equations for the *istantaneous variables*. In other words, ignore the stochastic nature of these variables and focus the attention on the physical relations that describe and relate them in space and time.

In the following sections, we will consider every variables composed by different terms. For example, the density and the potential temperature can be written as:

$$\rho_f = \underbrace{\rho_{00} + \rho_0(z)}_{\rho_a} + \underbrace{\overline{\rho}(\mathbf{x}, t) + \overline{\rho'}(\mathbf{x}, t)}_{\rho}$$

$$\theta_f = \underbrace{\theta_{00} + \theta_0(z)}_{\theta_a} + \underbrace{\overline{\theta}(\mathbf{x}, t) + \overline{\theta'}(\mathbf{x}, t)}_{\theta}$$

where (ρ_a, θ_a) are the values of the variable in hydrostatic condition (the first term is the reference value while the second is the variation over the height), and (ρ, θ) represent the dynamical variation of the variables, divided in average and turbulent terms (Tampieri [2010]).

Continuity Equation

Let's consider a parcel of air of volume V, enclosed by a lateral surface Σ (the vector normal to this surface is $d\Sigma$), with density ρ and crossed by a wind whose components are u, v and w.

The variation of mass of the parcel depends only by the outgoing flux from the surface Σ, so the equation of the *conservation of the mass* is:

$$-\frac{\partial}{\partial t} \iiint_V \rho_f \, dV = \iint_\Sigma (\rho_f v) \cdot d\Sigma \tag{1.18}$$

Supposing that the volume V doesn't change in time, using *Gauss theorem* and considering that the continuity equation must be valid for every volume

V, the equation can be re-written as:

$$\frac{\partial \rho_f}{\partial t} + \nabla(\rho_f v) = 0 \tag{1.19}$$

Remembering that the *divergence* of a vector is $\nabla \mathbf{v} = \partial u_j / \partial x_j$ and the definition of *total derivative* is $d/dt = \partial/\partial t + u_j \partial/\partial x_j$, the Eq. 1.19 can be transformed in:

$$\frac{d\,\rho_f}{d\,t} + \rho_f \frac{\partial u_j}{\partial x_j} = 0 \tag{1.20}$$

Considering that the air is in very good approximation an *incompressible fluid*, the first term of Eq. 1.20 is neglectable in respect to the second term ($d\rho_f/dt << \rho_f \partial u_j/\partial x_j$), so the continuity equation can be written as:

$$\frac{\partial u_j}{\partial x_j} = 0 \tag{1.21}$$

It is worth noting that when the approximation of incompressibility is valid, this relation turns into a *diagnostic* equation, non-time-dependent, meaning that the wind components have to always respect this condition during the entirety of the motion.

Conservation of a scalar

The equation for the conservation of a scalar quantity ς, such as the concentration of a chemical species or the potential temperature, can be obtained similarly to the continuity equation. The kinematic equation for the conservation of a quantity ς is:

$$\frac{\partial \varsigma}{\partial t} = -\frac{\partial F_i}{\partial x_i}$$

where F_i is the flux of ς, that can be expressed with *Fick's law* through the *coefficient of molecular diffusivity* specific for the considered variable κ_ς:

$$F_i = u_i \varsigma - \kappa_\varsigma \frac{\partial \varsigma}{\partial x_i}$$

Combining these two equations, a general expression for the conservation

of a scalar can be found, which can be written as follows:

$$\frac{\partial \varsigma}{\partial t} + u_j \frac{\partial \varsigma}{\partial x_j} = \kappa_\varsigma \frac{\partial^2 \varsigma}{\partial x_j x_j} \tag{1.22}$$

Therefore, in the case of the potential temperature, the appropriate constant is the thermic diffusivity χ, and the equation becomes:

$$\frac{\partial \theta}{\partial t} + u_j \frac{\partial \theta}{\partial x_j} = \chi \frac{\partial^2 \theta}{\partial x_j x_j} \tag{1.23}$$

Navier-Stokes equations

The *Navier-Stokes* equations (named after *Claude-Louis Navier* (1785-1836) and *Sir George Stokes* (1819-1903)) describe the motion of a fluid and arise from applying *Newton's second law* to the fluid.

Considering, as in the case of the continuity equation, a parcel of air of volume V enclosed by a lateral surface Σ, the time variation of momentum depends on the combined action of *volume forces* (acting on the entirety of the volume of the parcel) and *superficial forces* (acting on the surface of the parcel, representing the interaction with the air surrounding the parcel). This can be formalized with the following relation for a generic direction î:

$$\underbrace{\iiint_V \rho_f \frac{du_i}{dt}\, dV}_{\substack{\text{Variation of Momentum} \\ \text{in the volume V}}} = \underbrace{\iint_\Sigma T_i \cdot d\Sigma}_{SurfaceForces} + \underbrace{\iiint_V \rho_f G_i\, dV}_{VolumeForces} \tag{1.24}$$

where G_i is the i-th component of the external force $\mathbf{G}$ that acts on the whole volume, and T_i is a surface force (dependent on the fluid velocity) acting in the direction î.

Applying the *Gauss theorem*, it is possible to reformulate this equation like this:

$$\rho_f \frac{du_i}{dt} = \nabla T_i + \rho_f G_i \tag{1.25}$$

where all the vectors T_i represent the *stress tensor*, which describes the stress on the particles caused by the interaction with the fluid all around the parcel.

After expressing all the forces analytically, the Navier-Stokes equation can be written as follows:

$$\frac{\partial u_i}{\partial t} + u_j \frac{\partial u_i}{\partial x_j} = \underbrace{-\delta_{i3} g}_{(a)} + \underbrace{\varepsilon_{ij3} f u_j}_{(b)} - \underbrace{\frac{1}{\rho_f} \frac{\partial p_f}{\partial x_i}}_{(c)} + \underbrace{\nu \frac{\partial^2 u_i}{\partial x_j^2}}_{(d)} \tag{1.26}$$

The left-hand side of the equation is the total derivative (*lagrangian*) of the wind velocity component u_i, while the right-hand side terms are:

- *(a)*: gravitational term, limited only to the third component;
- *(b)*: *Coriolis effect*, describing the effect of the rotation of the Earth on the fluid;
- *(c)*: pressure term, describes the forces linked to the pressure gradient;
- *(d)*: viscous term, describes the influence of the viscous stress.

If we consider an homogeneous and in-quiet fluid, the Navies-Stokes equation represent the *hydrostatic equation*, that can be simplified as:

$$0 = \frac{1}{\rho_a} \frac{\partial p_a}{\partial x_i} + \delta_{i3} g \tag{1.27}$$

where p_a is the hydrostatic pressure (for a fluid in quite) and ρ_a the correspondent density.

Subtracting the hydrostatic equation to the Navier-Stokes equation (Eqs.1.26 and 1.27), we can finally write the equation for the dynamical part of the atmosphere:

$$\frac{\partial u_i}{\partial t} + u_j \frac{\partial u_i}{\partial x_j} = -\delta_{i3} g + f \, \varepsilon_{ij3} \, u_j - \frac{1}{\rho_{00}} \frac{\partial p}{\partial x_i} + \nu \frac{\partial^2 u_i}{\partial x_j^2} \tag{1.28}$$

1.5.2 Equation for the first moments

Using the Reynolds' hypothesis on the Navier-Stokes equations (Eq. 1.28) and applying the average operator on the result, it is possible to derive the

equation for the mean of the velocities components (from now on the Coriolis term will be neglected). This equation is called *Reynolds equation*, and reads:

$$\frac{\partial}{\partial t}\overline{u_i} + \overline{u_j}\frac{\partial \overline{u_i}}{\partial x_j} = -\frac{1}{\rho_{00}}\frac{\partial \overline{p}}{\partial x_i} + \nu\frac{\partial^2 \overline{u_i}}{\partial x_j \partial x_j} - \delta_{i3}\frac{g}{\rho_{00}}\overline{\rho} - \frac{\partial}{\partial x_j}\overline{u_i' u_j'} \tag{1.29}$$

Using the same methodology as for the previous equation, but on Eq. 1.23, the conservation of the potential temperature can be expressed as:

$$\frac{\partial \overline{\theta}}{\partial t} + u_j\frac{\partial \overline{\theta}}{\partial x_j} = \chi\frac{\partial^2 \overline{\theta}}{\partial x_j x_j} - \frac{\partial}{\partial x_j}\overline{u_j'\theta'} \tag{1.30}$$

We can thus see that, as a consequence of the Reynolds' hypothesis and the averaging process, it has been introduced in each of the previous equations a new term of the second order. This causes the set of equations to be *not closed*, because we would always need an additional term of an high order to solve any of the equations.

1.5.3 Equation for the second moments

As seen in the previous section, all the first order equations contain a term of the second order, so we need to find an expression for those as well. After a series of long but straightforward calculations, we can write the equation for the second moments of the momentum:

$$\begin{aligned}\frac{\partial \overline{u_i' u_k'}}{\partial t} + \overline{u_j}\frac{\partial \overline{u_i' u_k'}}{\partial x_j} = &-\left(\overline{u_i' u_j'}\frac{\partial \overline{u_k}}{\partial x_j} + \overline{u_k' u_j'}\frac{\partial \overline{u_i}}{\partial x_j}\right) - \frac{\partial \overline{u_i' u_j' u_k'}}{\partial x_j} \\ &- \frac{g}{\rho_{00}}\left(\delta_{k3}\overline{u_i'\rho'} + \delta_{i3}\overline{u_k'\rho'}\right) \\ &- \frac{1}{\rho_{00}}\left(\overline{u_k'\frac{\partial p'}{\partial x_i}} + \overline{u_i'\frac{\partial p'}{\partial x_k}}\right) \\ &+ \nu\frac{\partial^2 \overline{u_i' u_k'}}{\partial x_j \partial x_j} - 2\nu\overline{\frac{\partial u_i'}{\partial x_j}\frac{\partial u_k'}{\partial x_j}}\end{aligned} \tag{1.31}$$

The meaning of the different terms is:

- The first term is the product of the covariances of the wind components fluctuations (in other terms, the flux of momentum as we demonstrated in Section 1.4.2) and the gradient of the mean wind components, and it represents the production of momentum from the mean shear of the wind.

- The second term is a third order moment, and it represents the transport of momentum due to the turbulence.

- The third term is the coupling between the fluctuations of density and velocity and represents the creation/removal of momentum due to the turbulence.

- The fourth term is also a third order moment (because the pressure scales on the square of the velocity), and it represents the transport of momentum.

- The fifth term is composed by the molecular diffusion of the second order moment $\overline{u_i' u_k'}$ and the correlation between the gradients of the velocity fluctuations. Considering the turbulence at small scale homogeneous and isotropic, in the latter term the components of the product with $i \neq k$ disappear, so we can approximate this term to:

$$\varepsilon = \nu \overline{\left(\frac{\partial u_i'}{\partial x_j} \right)^2}$$

  which is a (always positive) term, representing the molecular destruction of momentum due to the viscosity of the fluid.

Using Eq. 1.31 with the condition $i = k$, we can find an expression for the evolution of the Turbulent Kinetic Energy, which we defined in Section 1.4.1 as $TKE = 1/2\,\overline{u_i' u_i'}$, and the equation reads:

$$\frac{d(TKE)}{dt} = -\overline{u_i'u_j'}\frac{\partial \overline{u_i}}{\partial x_j} - \frac{1}{\rho_{00}}\frac{\partial \overline{p'u_j'}}{\partial x_j} - \frac{1}{2}\frac{\partial \overline{u_i'u_i'u_j'}}{\partial x_j} - \frac{g}{\rho_{00}}\delta_{i3}\overline{\rho'u_i'} - \nu\frac{\partial^2(TKE)}{\partial x_j \partial x_j} - \varepsilon \tag{1.32}$$

In this equation the term $-\overline{u_i'u_j'}\frac{\partial \overline{u_i}}{\partial x_j}$ is the *mechanical generation of turbulence* due to wind shear, while the fourth term $\frac{g}{\rho_{00}}\delta_{i3}\overline{\rho'u_i'}$ is the *buoyant production or destruction of turbulence* due to heat fluxes. The other terms are either *transport of turbulence* (second and third terms) or viscous *dissipation of turbulence*.

The balance between the terms of generation and consumption of turbulence tells us if TKE is been produced or dissipated, and the ratio of these two terms defines the dimensionless *flux Richardson number* R_f, which can be written:

$$R_f = \frac{\frac{g}{\rho_{00}}\overline{\rho'w'}}{\overline{u_i'u_j'}\frac{\partial \overline{u_i}}{\partial x_j}} = \frac{\frac{g}{\theta_{00}}\overline{w'\theta'}}{\overline{u_i'u_j'}\frac{\partial \overline{u_i}}{\partial x_j}} \tag{1.33}$$

Similarly to the case of the momentum, the equation for the variance of a scalar can be derived (in this case, the potential temperature θ):

$$\frac{\partial \overline{\theta'^2}}{\partial t} + \overline{u_j}\frac{\partial \overline{\theta'^2}}{\partial x_j} = -2\overline{u_i'\theta'}\frac{\partial \overline{\theta}}{\partial x_i} - \frac{\partial \overline{u_i'\theta'^2}}{\partial x_i} + \chi\overline{\theta'\frac{\partial^2\theta'}{\partial x_i \partial x_i}} \tag{1.34}$$

As we saw, the correlation between the velocity and the temperature can be associated to the (cinematic) heat flux $\overline{u_i'\theta'}$. In particular, the equation for the vertical flux ($i = 3 \rightarrow u_i = w$) is:

$$\frac{\partial \overline{w'\theta'}}{\partial t} + \overline{u_j}\frac{\overline{w'\theta'}}{\partial x_j} = -\overline{u_j'w'}\frac{\partial \overline{\theta}}{\partial x_j} + \frac{g}{\theta_{00}}\overline{\theta'^2} - \frac{\partial \overline{w'u_j'\theta'}}{\partial x_j} - \frac{1}{\rho_{00}}\overline{\theta'\frac{\partial p'}{\partial z}} \tag{1.35}$$

In all the previous equations we can see that there is at least a term of the third order, proving once again that, using the Reynolds' hypothesis, this set of equations is not *closed*.

1.5.4 Closure problem

We saw that if we try to describe any equation of the generic n-th order, due to the non-linearity of the fluid-dynamics' equations, we must introduce a term of the (n+1)-th order. Mathematically speaking, this means the equations are not closed, we always need an infinite amount of equations to describe the turbulence.

To mitigate this difficulty, we can make *closure assumptions*. Namely, we can retain a finite number of equations and then approximate the remaining unknowns as a function of the knowns. The resulting *parameterization* will not give a perfect answer, but it will give an approximate answer that often is good enough.

One can categorize the turbulence closure assumptions with their *statistical order*, named after the highest order forecast equation retained. A common, local first-order closure is called *eddy diffusivity theory* or *K-theory*, which assumes (similarly to molecular diffusion) that the flux is linearly proportional to and directed down the local gradient, so in the case of heat and momentum fluxes:

$$\overline{w'\theta'} = -K_h \frac{\partial \overline{\theta}}{\partial z} \tag{1.36}$$

$$\overline{u'w'} = -K_m \frac{\overline{\partial \overline{u}}}{\partial z} \tag{1.37}$$

where the eddy diffusivities, K_m and K_h, are used instead of the molecular diffusivity. The closure in Eq. 1.36 is a local closure in the sense that the heat flux at any altitude depends on the local flux at that same altitude. Namely, it implicitly assumes that only small-size eddies exist.

1.6 Similarity Theory

The experimental observations of the meteorological quantities that describe the PBL often show repeatable characteristics, suggesting the possibility of developing semi-empiric relationships between them. This is obviously very important, because of all the different closure models that always require new connections between different variables.

This hypothesis has had a very unexpected success, introducing the idea of finding a totally semi-empiric description of the PBL, but valid (at least in first approximation) in most cases.

In theory, there are an infinite number of subjective ways in which to find diagnostic semi-empiric relationships (only describing the spatial evolution, not the time evolution). In this regard, an objective and rigorous methodology has been developed, based on *dimensional analysis*, called *similarity theory*. This theory is based on the Π -*Theorem* or *Buckingham Theorem*, which allows the organization of different variables in a logical and unique way (Sozzi et al. [2002]).

The *similarity analysis* is based on four separate steps:

- Selection of the variables that are considered important
- Organization of these variables in *adimensional groups*
- Execution of experiments, or data analysis of previously made experiments, in order to determine the value of these non-dimensional groups
- Determination of analytic relations in order to quantitatively describe the connections between the groups

The entire theoretical construct is based on the *dynamical similarity* concept, which states that two fluids are dynamically similar if it is possible to describe one knowing the experimental characteristic of the other. The procedure described above tends to collapse similar situations in a more generalized and universal one, identifying which adimensional groups of variables define it.

1.6.1 The Buckinghan Theorem

In 1914, Buckingham proposed a systematic approach in order to analyze experimental measurements, consisting in a series of steps here illustrated.

Step 1:

Identify all the *fundamental variables* of interest and their dimensions. This is a very delicate step that requires a careful theoretical and experimental knowledge of the problem.

Step 2:

Identify a subset of the fundamental variables (the *key variables*), which must satisfy the following restrictions:

- the number of key variables must be equal to the number of the fundamental variables;
- all the dimensions found for the fundamental variables must be present in the key variables subset;
- it must be impossible to create non-dimensional variables combining the key variables.

Step 3:

Write the equations for the non-key variables (NK_i) expressed in function of the key variables (K_i) in the form of the product of powers of the key variables, i.e.:

$$\begin{aligned} [NK_1] &= [K_1]^{a_1}[K_2]^{b_1}\dots[K_i]^{n_1} \\ [NK_2] &= [K_1]^{a_2}[K_2]^{b_2}\dots[K_i]^{n_2} \\ &\vdots \\ [NK_m] &= [K_1]^{a_m}[K_2]^{b_m}\dots[K_i]^{n_m} \end{aligned} \tag{1.38}$$

Find the correct values for the exponents so that the previous equations are verified.

Step 4:

Take the ratio between the LHS and the RHS of each equation, ob-

taining non-dimensional groups (Π). The number of non-dimensional groups will always be the number of the fundamental variables minus the numbers of the key variables, hence reducing the number of independent variables.

It is possible to introduce different non-dimensional groups combining the existing one, keeping in mind that:

- The number of variables cannot change;
- All the key variables must be present;
- The groups must be independent.

After this analysis, the result is that we can expect to find semi-empiric relationships between these non-dimensional groups, which can be found experimentally.

1.6.2 The Monin-Obukhov Similarity Theory (MOST)

A very important application of the similarity theory is in the Surface Layer, that is the lowest layer of the PBL where the fluxes can be considered constant (i.e. they vary less than 10%). Considering spatially homogeneous and stationary conditions and orientating the frame of reference with the wind streamline, we are interested in investigating the possibility of describing in universal terms the vertical profile of the main variables that describe the turbulence (i.e. wind shear $\frac{du}{dz}$, thermal stratification $\frac{d\theta}{dz}$, etc.).

Following the steps of the Buckingham Theorem, Monin and Obukhov [1954] used as fundamental variables:

- z: the height inside the Surface Layer;
- $u_* = (\overline{u'w'}^2 + \overline{v'w'}^2)^{\frac{1}{4}}$: *friction velocity*: indicator of shear turbulence
- $\overline{w'\theta'} = u_*\theta_*$: indicator of thermal turbulence (θ_* temperature scale);
- $\beta = \frac{g}{\theta_0}$: buoyancy parameter;
- f: generic variable of which we are interested in its vertical profile.

Amongst all these variables, it is possible to define two different non-dimensional groups, the first is a scale length $\zeta = \frac{z}{L_{MO}}$, where L_{MO} is the Monin-Obukhov length defined as:

$$L_{MO} = -\frac{u_*^3}{\frac{\kappa g}{\theta_{00}}\overline{w'\theta'}} \tag{1.39}$$

and the second variable is $\frac{f}{f_0}$, where f_0 has the same dimensions of f and is defined using the other fundamental variables. This variable depends on the ratio between the shear (mechanical) and thermal turbulence, therefore it can be used as a stability discriminant. In fact, considering what has been said in Section 1.4.2, while $u_* > 0$, $w'\theta'$ depends on stability, therefore if positive we are in a convective situation ($L_{MO} < 0$), otherwise we are in a stable situation ($L_{MO} > 0$).

The absolute value of L_{MO} can be taken as the height where there is balance between the turbulent fluxes of heat and momentum. In other words, for $z < |L_{MO}| \rightarrow |\frac{z}{L_{MO}}| < 1$ the shear turbulence predominates the PBL, while for $z > |L_{MO}| \rightarrow |\frac{z}{L_{MO}}| > 1$ the thermal turbulence prevails.

From these observations, the Monin-Obukhov similarity theory states that, in general, it is possible to find (for every variable f that describes the turbulence in the surface layer) only one universal vertical profile, expressed by the following relation:

$$\frac{f}{f_0} = F_f(\zeta) \Rightarrow f = f_0 \cdot F_f(\zeta) \tag{1.40}$$

where $F_f(\zeta)$ is the *universal similarity function* for the variable *f*. Of course, the dimensional analysis does not provide the form of these universal functions; that can be found only through experiments.

1.6.3 Similarity Functions for the wind Shear and Profile

If we consider the wind shear $\frac{du}{dz}$, it is easy to define the variable f_0 as $\frac{u_*}{\kappa z}$. Therefore, we can write equation (1.40) as:

$$\frac{du}{dz} = \frac{u_*}{\kappa z}\phi_m(\zeta) \tag{1.41}$$

where $\phi_m(\zeta)$ is the universal similarity function for the wind shear.

Integrating the previous equation (between z_{0m} and z), one can obtain the function for the wind profile, expressed by the following equation:

$$u(z) = \frac{u_*}{\kappa}\int_{z_{0m}}^{z}\frac{\phi(\zeta)}{z}dz \tag{1.42}$$

which can be written in this form:

$$u(z) = \frac{u_*}{\kappa}\left[ln\left(\frac{z}{z_{0m}}\right) - \Psi_m(\zeta,\zeta_{0m})\right] = \frac{u_*}{\kappa}\Upsilon_m(\zeta,\zeta_{0m}) \tag{1.43}$$

where $\zeta = \frac{z}{L_{MO}}$ and $\zeta_{0m} = \frac{z_{0m}}{L_{MO}}$ and

$$\Psi_m(\zeta) = \int_{\zeta_{0m}}^{\zeta}\left[1-\phi_m(\zeta)\right]\cdot\frac{d\zeta}{\zeta} \tag{1.44}$$

Eq. 1.43 is the *universal similarity function for the wind profile*, and $\Psi_m(\zeta)$ is called the *universal relative similarity function.*

The analytical form of the *universal similarity functions* ϕ_m and Ψ_m has been determined by numerous field campaigns and experiments.

1.6.4 Similarity Functions for the Temperature Gradient and Profile

Similar consideration can be done regarding the potential temperature gradient $\frac{d\theta}{dz}$, hence in this case Eq. 1.40 can be written as:

$$\frac{d\theta}{dz} = -\frac{\theta_*}{\kappa z}\phi_h(\zeta) \tag{1.45}$$

where $\phi_h(\zeta)$ is the universal similarity function for the temperature gradient. Again, the previous equation can be integrated (between the limit z_{0h} and z), and the final form is:

$$\theta(z) - \theta(z_{0h}) = -\frac{\theta_*}{\kappa}\left[ln\left(\frac{z}{z_{0h}}\right) - \Psi_h(\zeta)\right] = -\frac{\theta_*}{\kappa}\Upsilon_h(\zeta, \zeta_0) \tag{1.46}$$

Eq. 1.46 is the *universal similarity function for the mean potential temperature* and $\Psi_h(\zeta)$ is the *universal relative similarity function.*

Again, the analytical form of the *universal similarity functions* ϕ_h and Ψ_h has been determined by numerous field campaigns and experiments.

1.6.5 Richardson Numbers

We already defined in Section 1.5.3 the *flux Richardson number.* Combining the definitions of R_f (Eq. 1.33), of the friction velocity u_*, and the similarity function for the wind shear (Eq. 1.41), we can see that:

$$R_f = \frac{\frac{g}{\theta_{00}}\overline{w'\theta'}}{\overline{u'w'}\frac{d\overline{u}}{dz}} = \frac{\frac{g}{\theta_{00}}\overline{w'\theta'}}{(-u_*^2)\frac{u_*}{\kappa z}\phi_m(\zeta)} = \zeta\phi_m^{-1}(\zeta) \tag{1.47}$$

which allows us to take the Richardson number as a stability parameter.

Considering that sometimes the measurements of the fluxes can be difficult, it is possible to consider instead the gradient of temperature and wind speed, easier to obtain in a field experiment. In order to achieve this, it is possible to use the flux-gradient relationships defined in Chapter 1.5.4 directly in the definition of R_f:

$$R_f = \frac{g}{\theta_{00}}\frac{\overline{w'\theta'}}{\overline{u'w'}\frac{d\overline{u}}{dz}} = \frac{g}{\theta_{00}}\frac{K_h\frac{\partial\overline{\theta}}{\partial z}}{K_m\left(\frac{\partial\overline{u}}{\partial z}\right)^2}$$

from which it is possible to define the *gradient Richardson number* as:

$$R_g = \frac{g}{\theta_{00}}\frac{\frac{\partial\overline{\theta}}{\partial z}}{\left(\frac{\partial\overline{u}}{\partial z}\right)^2} \tag{1.48}$$

Using the similarity functions for the wind shear (Eq. 1.41) and the temperature gradient (Eq. 1.45), we can write another formulation of R_g which depends on the stability:

$$R_g = \frac{g}{\theta_{00}} \frac{\frac{\partial \overline{\theta}}{\partial z}}{\left(\frac{\partial \overline{u}}{\partial z}\right)^2} = \frac{g}{\theta_{00}} \frac{-\frac{\theta_*}{\kappa z}\phi_h(\zeta)}{\left(\frac{u_*^2}{\kappa z}\right)^2 \phi_m^2(\zeta)} = \zeta \frac{\phi_h(\zeta)}{\phi_m^2(\zeta)} \tag{1.49}$$

It is also possible to evaluate the Richardson number if there are only discretized measurements of wind and temperature (temperature at z_1, z_2 and wind at z_3, z_4). In this case it is called *bulk Richardson number*, and we can replace the wind and temperature gradients with finite differences (e.g. $\frac{d\overline{u}}{dz} = \frac{\Delta \overline{u}}{\Delta z}$) to obtain:

$$R_b = \frac{g}{\theta_{00}} \frac{\theta(z_1) - \theta(z_2)}{\left[u(z_3) - u(z_4)\right]^2} \cdot \frac{(z_3 - z_4)^2}{z_1 - z_2}$$

Using the similarity functions for the profiles (Eqs. 1.43 and 1.46), we can write a stability dependent formulation for R_b:

$$R_b = \frac{1}{L_{MO}} \frac{\Delta z_m^2}{\Delta z_h} \frac{\Upsilon_h(\zeta, \zeta_{0h})}{\Upsilon_m^2(\zeta, \zeta_{0m})} \tag{1.50}$$

Chapter 2

Data Analysis

2.1 Origin of the data: SABLES98

The entirety of the data used in this work originated from a campaign experiment called Stable Atmospheric Boundary Layer Experiment in Spain (henceforth SABLES98). This experiment took place at the Research Centre for the Lower Atmosphere (CIBA) over the northern Spanish plateau (the Torozos plateau), in the period 10-28 September 1998. This center belongs to the University of Valladolid and the Spanish Meteorological Institute (INM), and has been previously used for a number of experiments related to research on the atmospheric boundary layer (Cuxart et al. [2000]). The purpose of the experiment was to study the characteristic of the Stable Boundary Layer in mid-latitudes in fairly-flat and homogeneous conditions. It is possible to see a schematic representation of the position of the CIBA site in Fig. 2.1, and a schematic cross section of the Torozos plateau in Fig. 2.2.

Even though the campaign took place over a period of 18 days, only the days between the 14th and the 21st of September were considered to be the best for studying the SBL. During these days, the Azores high pressure system extended over Spain, and the general situation was quite stationary, with weak synoptic winds from the north-east which tend to increase at the end of the period.

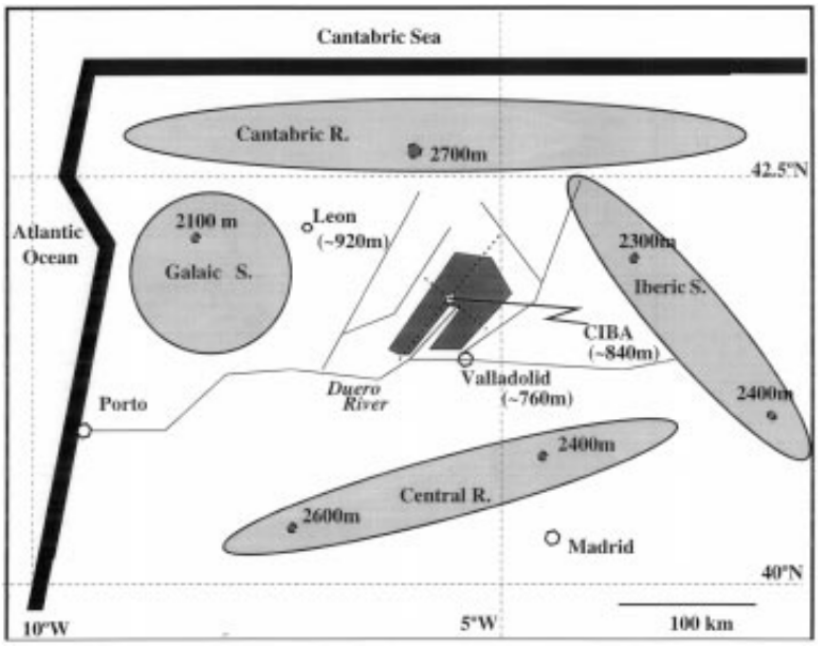

Figure 2.1: *Location of the CIBA site within a schematic description of the topographical features of the north-western Iberian peninsula. The light shaded areas are mountain ranges, while the dark shaded area is the Torozos plateau (Cuxart et al. [2000]). The short dashed lines over the plateau area are the cross sections for Fig.2.2.*

All data was collected into a vast database. For each day the recorded measurements went from 18:05 to 05:50 (Local Time, GMT+2), with an averaging period of 5 minutes.

In order to collect the data, two meteorological masts were available at the CIBA site, with heights of 100 m and 10 m. High precision meteorological instruments were mounted on these masts, and a list of these instruments and their height from the ground is given below (Cuxart et al. [2000]).

- The 100 meter mast was instrumented with a vertical array of 15 thermocouples (0.22m, 0.88m, 2m, 3.55m, 5.55m, 8m, 10.88m, 14.22m, 18m, 22.22m, 26.88m, 32m, 37.55m, 43.55m, 50m), three sonic anemometers (5.8m, 13.5m, 32m), a fast humidity sensor (13.5m), an infrared surface temperature sensor (2m), a radiometer (2m) and a barometer (surface). In addition, lower response measurements were made of wind

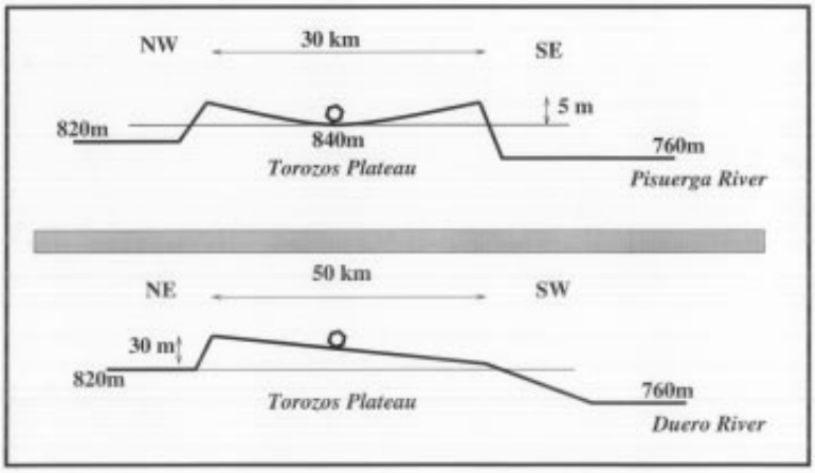

Figure 2.2: *Upper diagram: north-west to south-east schematic cross section of the Torozos Plateau; lower diagram: north-east to south-west schematic cross section (Cuxart et al. [2000]).*

speed (3m, 10m, 20m, 50m, 100m), wind direction (10m, 20m, 100m), temperature (10m, 20m, 50m) and humidity (3m, 20m).

- The goal of the equipment on the 10 meter mast was to give measurements within the surface layer. Low response instruments were used to measure temperature, humidity, wind speed and direction at three different levels (2.5m, 5.5m, 10m). In addition, two sonic anemometers (3.5m, 7.5m) and two net radiometers (1m, 6m) were also deployed.

- A triangular array of cup anemometers was installed, at a height of 1.5m from the ground. The purpose of this array was to detect gravity waves, however at times the wind speed was so low that not much information could be obtained from them.

2.2 Surface Roughness Length z_0

From the similarity equations 1.43 and 1.46, we introduced a pair of constants during the integration process, called respectively z_{0m} and z_{0h}. These are basically the heights that give us the lower limits of integration for the two similarity functions for the wind and the temperature profiles. Even though these two constants are not necessarily equal, they are very often considered so, and they are called just *Surface Roughness Length* z_0 (Mahrt [1998]).

This number represents the height over the ground where wind and temperature reach their surface value, height that is not always zero due to the roughness of the surface (hence the name). This number is very small, much smaller than a meter, usually of the order of the centimeter, depending on the type of surface (farmland, grass, crops, etc.).

It is possible to evaluate these constants taking into account the behaviour of the similarity functions in proximity to the ground. In this *surface layer*, the vertical profiles of wind and potential temperature are well described by the Monin-Obukhov similarity theory (as seen in Chapter 1.6.2). It is interesting to note that, if the parameter $z/L_{MO} \to 0$, all the relations are less dependent on stability, and they become logarithmic profiles ($\Phi(\zeta) \to 1$).

The universal similarity functions for the wind shear (equation 1.43) and for the temperature profile (equation 1.46) will read:

$$u(z) = \frac{u_*}{\kappa} ln\left(\frac{z}{z_{0m}}\right) \tag{2.1}$$

$$\theta(z) - \theta(z_{0h}) = -\frac{\theta_*}{\kappa} ln\left(\frac{z}{z_{0h}}\right) \tag{2.2}$$

It is now possible to invert these formulas in order to evaluate the *surface roughness* z_{0m} and z_{0h}, considering of course only cases close to *neutrality*. In fact, as we defined in Chapter 1.2, the boundary layer approaches neutrality when the thermal exchanges between air and surface are minimal, namely when the thermal fluxes approaches zero ($\overline{w'\theta'} \to 0$). If we use this in the definition of the stability parameter $\zeta = z/L_{MO}$ (Eq. 1.39), we find that neutrality is achieved when $\zeta \to 0$. For the analysis we considered only

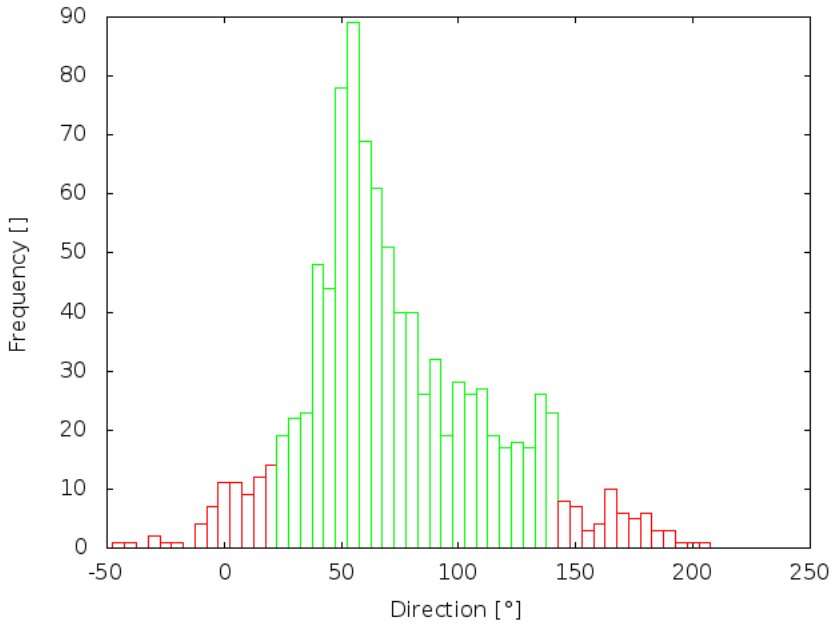

Figure 2.3: *Histogram of the frequencies of the wind's directions throughout the entire period. The green bars indicate the directions considered in the z_{0m} analysis.*

values of $1/L_{MO} < 0.03$ at an height $z = 5.8m$.

Observing the topographical features of the territory around the CIBA site (Fig. 2.2), it is reasonable to assume that z_{0m} could depend on the direction from which the wind is blowing. In order to analyze this problem, we divided the set of directions found in the data in intervals of 5 degrees, from -50 (north-westerly winds) to 250 (south-westerly winds), and plotted a histogram (Fig. 2.3). From here it is possible to see that the main directions from which the wind is blowing throughout the seven days of observation can be taken between 15 (north-east) and 145 (south-east).

With this information, using as parameters $k = 0.4$ (the Von Karman constant), $\overline{u}(z)$ and $u_*(z)$ from the dataset, and with $z = 5.8$, it is possible to evaluate z_{0m} for each time step. The characteristic value of z_{0m} for the CIBA site has then been evaluated as $z_{0m} = 0.049m$, taking the average of all of them (Fig. 2.4). We repeated the same procedure in order to calculate z_{0h}. In this case the data was much more scattered, mainly because the

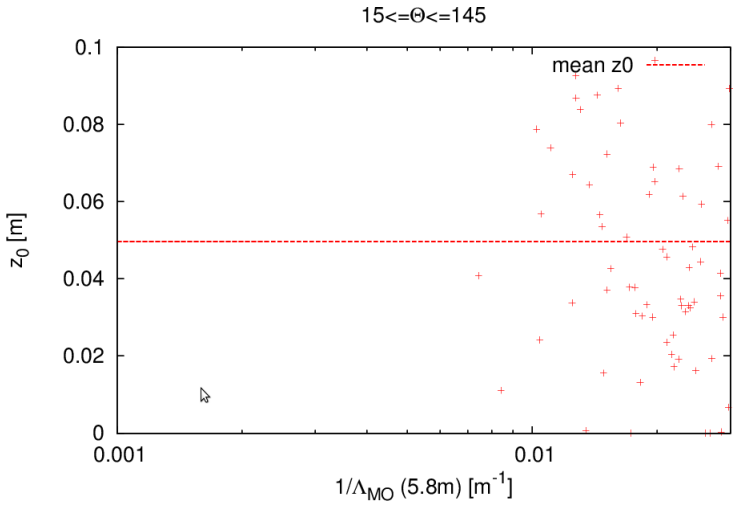

Figure 2.4: *Values of z_{0m} in near-neutral conditions. The horizontal line represents the calculated average value of $z_{0m} = 0.049m$.*

values of θ_* in this range of stability is very close to zero. Although, we approximated a value of about $z_{0h} \simeq 0.0003m$. The ratio between the two surface roughness is $z_{0m}/z_{0h} \simeq 160$. Calculation of z_{0h} is very sensitive to how the surface temperature are measured (Edwards [2009]). Common estimates of this ratio (Luhar et al. [2009], Garratt [1992]) are with order of magnitude between $10 \div 10000$.

2.3 Vertical structure of the SBL

Following Mahrt [1999] *"any attempt to divide the stable boundary layer into a few classes or states is an oversimplification"*. The classes that we are going to use in this study must be taken as prototypes and must be considered as an attempt to find some organization in the study of the stable boundary layer.

Boundary-layer meteorology has long distinguished between cases of *traditional stable boundary layer* with continuous turbulence, and those with stronger stability and often intermittent turbulence (Mahrt [1998], Grachev et al. [2005], Sorbjan and Grachev [2010]). In the first case, generation of turbulence is due to surface roughness and its transport is upward or weak. The

thermal and momentum fluxes decrease with height and become small near the top of the SBL. In the second case, instead, the vertical structure does not satisfy the traditional concept of boundary layer, and surface-based processes are not the main driving mechanisms to the generation of turbulence. This in fact can be generated at higher levels above the ground, causing the fluxes to increase with height, and granting this class of SBL the name of *upside-down boundary layer* (Mahrt and Vickers [2002]).

To classify these different types of boundary layers, we considered the vertical profiles of thermal and momentum fluxes measured at three heights ($5.8m$, $13.5m$, and $32m$), in order to define different *cases* based on how the slopes of the fluxes behave. With only three levels available and defining "slope down" the slope in the lower layer (between $5.8m$ and $13.5m$), and "slope up" the slope in the top layer (between $13.5m$ and $32m$), it is possible to define four different cases:

- Case 1: $slope\ down < 0$ and $slope\ up < 0$
- Case 2: $slope\ down < 0$ and $slope\ up > 0$
- Case 3: $slope\ down > 0$ and $slope\ up < 0$
- Case 4: $slope\ down > 0$ and $slope\ up > 0$

The first case, with fluxes decreasing with height, is characteristic of a *traditional* SBL, while the last one, with fluxes increasing with height, is representative of an *upside-down* SBL. The other two cases are intermediate situations, and they are not easily definable as traditional or upside-down without further investigations.

2.4 Time Series

Time series of the main variables that we have available are a useful tool to help visualize at first sight how the SBL is behaving. In this section we are going to show some of the time series extrapolated from the dataset and show

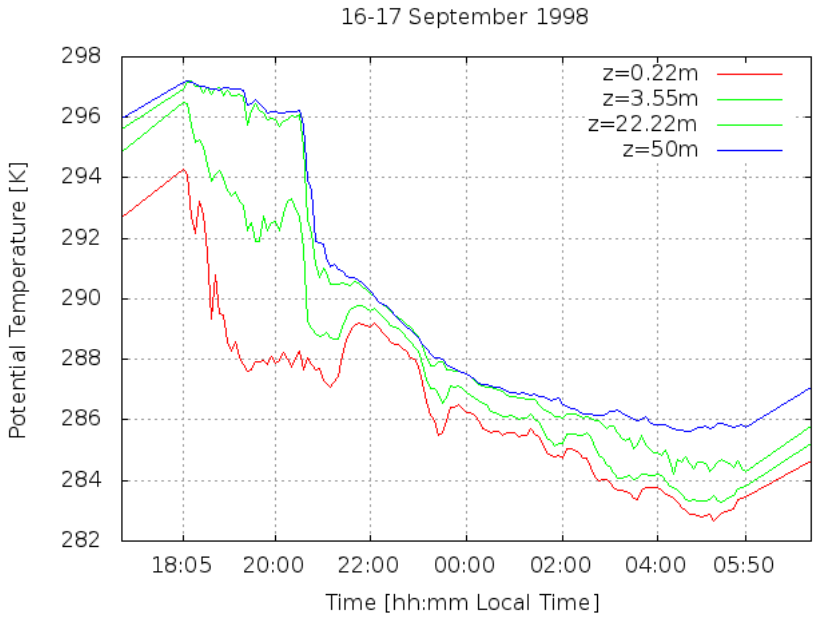

Figure 2.5: *Time series of the potential temperature over the period 16-17 September 1998.*

how it is possible to identify if the SBL is in a traditional or upside-down state.

Considering only data from the third night of the experiment (between 16-17 September), we can see in Fig. 2.5 the time series of the potential temperature at different heights ($0.22m$, $3.55m$, $22.22m$ and $50m$). It is possible to notice that θ increases with height, with a stronger gradient near the ground, while toward higher levels the increase slows down. This is compatible with a typical nocturnal situation, where the ground cools faster than the atmosphere and the top of the SBL meets the residual well-mixed layer.

In Fig. 2.6, it is shown the time series of the wind speed for the same time period. We can see here that the wind is stronger at higher levels, and very weak near the ground, in accordance with the no-slip condition. It is possible to notice an abrupt increase in the velocity at the highest level ($100m$), which could indicate the presence of a *low-level jet (LLJ)*. It is also possible to note that a decrease in the potential temperature occurred at approximately the

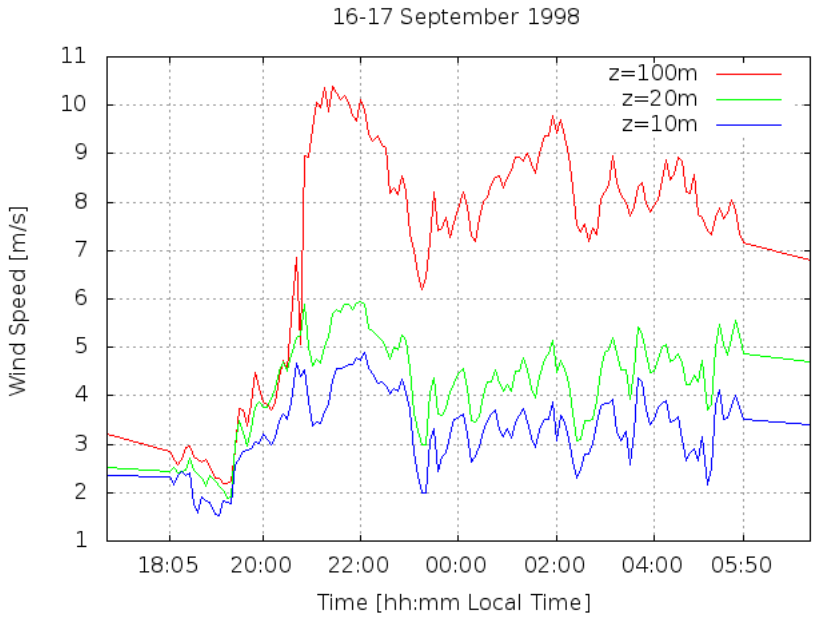

Figure 2.6: *Time series of the wind speed over the period 16-17 September 1998.*

same time as the increase of the wind speed.

The next graph (Fig. 2.7) shows the time series of the gradient Richardson number. Here it is very apparent that the changes in wind speed and/or potential temperature noted before had some influence on the stability of the SBL. In fact, after those changes, R_g decreased significantly at all heights to values closer to zero, near neutral conditions.

In Fig. 2.8 is shown the turbulent kinetic energy TKE. This parameter is used to detect where the turbulence is generated: in case of a traditional SBL it decreases with height, while it can increase if turbulence is produced aloft, as in the case of an upside-down boundary layer. In this graph we can see, corresponding to the abrupt increase of wind speed, an evident increase in production of turbulence. The TKE, in fact, goes from values or the order of 10^{-2} to values of an order of magnitude bigger, around $0.2 - 0.5$.

In the same graph, it is easy to notice that the TKE decreases with height toward the end of the night (after 03:00 LT), suggesting that the SBL is in a traditional state. To verify this, it is possible to overlay an indicator of the

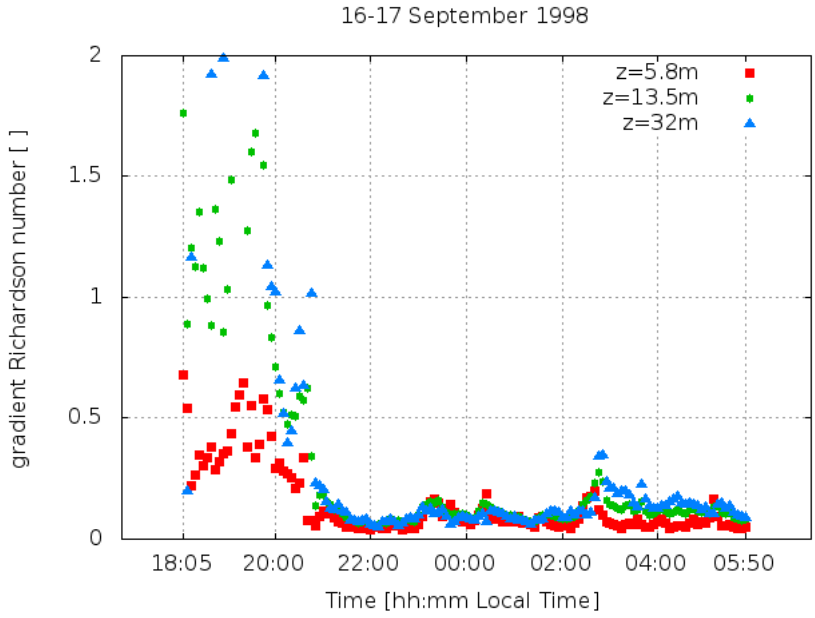

Figure 2.7: *Time series of the gradient Richardson number R_g over the period 16-17 September 1998.*

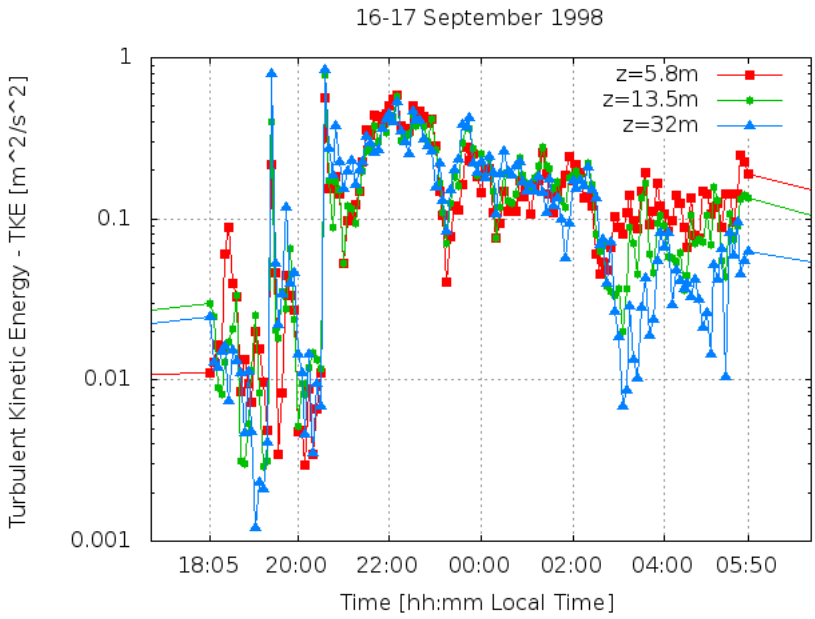

Figure 2.8: *Time series of the turbulent kinetic energy TKE at three different heights (5.8m, 13.5m and 32m) over the period 16-17 September 1998.*

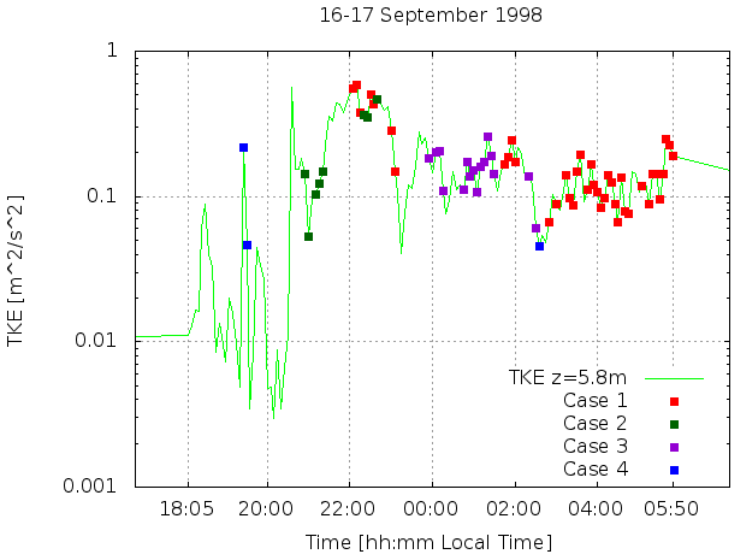

Figure 2.9: *Time series of the turbulent kinetic energy TKE at 5.8m over the period 16-17 September 1998. Plotted on the graph there are indicators for the different cases which can define the state of the SBL. Where no points are shown, the fluxes couldn't be calculated or the heat and momentum fluxes didn't have the same behaviour.*

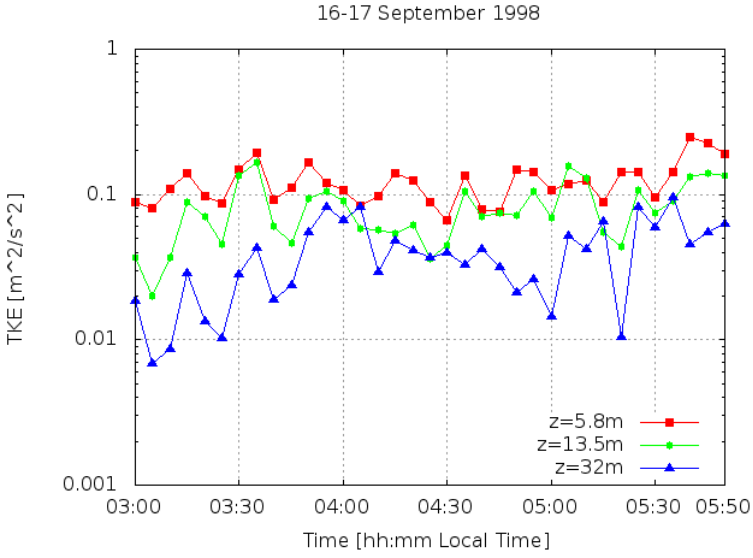

Figure 2.10: *Like Fig. 2.8 but only the time period 03:00-05:50 Local Time.*

Figure 2.11: *Time series of the TKE at 00:00-02:00 LT, 16-Sep during an upside-down SBL.*

cases that we defined in Chapter 2.3 on the graph. We already stated that in a traditional SBL, the thermal and momentum fluxes should decrease with height, so we are going to indicate on the graph only the cases where both of these quantities have the same behaviour with height. It is possible to see in Fig. 2.9 that in the period considered, the fluxes are in fact decreasing. Therefore, the SBL can be considered in a traditional state.

During the study of the various time series, we noted that this type of boundary layer appears more often than its upside-down counterpart. Nonetheless, during the second night of observations (16 September, 00:00-02:00), a period when the fluxes and the kinetic energy are increasing with height is visible. In Fig. 2.11 is shown the time series of the TKE, which assumes average values of $0.02m^2/s^2$ at $5.8m$, $0.04m^2/s^2$ at $13.5m$ and $0.06m^2/s^2$ at $32m$. Therefore in this period the boundary layer can be considered in an upside-down state.

2.5 Vertical Profiles

We stated before that the two main states in which we can find the SBL are the *traditional* and the *upside-down* states. In this section, we are going to analyze some vertical profiles of different variables, differentiating these two cases.

During the different analysis, we noticed that the thermocouples mounted on the $100m$ mast at the heights of $2m$ and $18m$ are probably damaged and the measurements are incorrect. For this reason, all the data taken at these two levels have been discarded.

2.5.1 Traditional Boundary Layer

In the previous section we noted that, toward the end of the third night of observation (17th of September, 03:00-05:50 Local Time), a decrease in

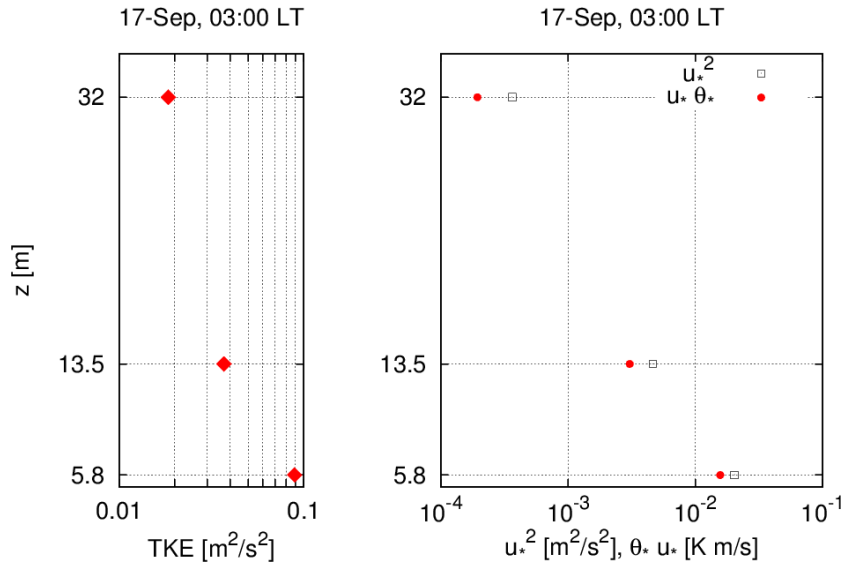

Figure 2.12: *(a) Left panel: profile of the TKE at 03:00 LT, 17-Sep. (b) Right panel: profile of the momentum flux (u_*^2) and the thermal flux ($|\theta_* u_*|$) at 17-Sep, 03:00 LT.*

the TKE with height is visible, on average $0.12m^2/s^2$ at $5.8m$, $0.07m^2/s^2$ at $13.5m$ and $0.03m^2/s^2$ at $32m$ (Fig. 2.8, Fig. 2.10 for a close-up). In Fig. 2.12, we can see an example of the profiles of the turbulent kinetic energy and of the fluxes of momentum and heat taken at the beginning of the period (03:00 LT). The heat flux should be negative ($\theta_* < 0$), so we plotted the absulute value of the thermal flux to have a better comparison. It is immediately apparent that they decrease with height, therefore we can consider this portion of the night as representative of a traditional boundary layer.

In the next figure (Fig. 2.13), we can see the potential temperature profiles at two different times, at the beginning and the end of the considered period. It is possible to note how the ground is cooler than the atmosphere above, and that, as time passes, the temperatures decrease at every level but remain almost constant at the top, connecting to the residual well-mixed layer above.

Different methods have been developed in order to estimate the height of the stable boundary layer (Zilitinkevich and Baklanov [2002]). The charac-

teristic of the temperature profile described above allows us to estimate the so-called *temperature height* h_t of the stable boundary layer. In fact, knowing that the residual layer above the SBL is what remains of the diurnal well-mixed convective boundary layer, we can assume that said temperature is almost constant. Calculating the derivative of the potential temperature profile, we can evaluate h_t as the height at which the slope of the potential temperature tends to zero. Fig. 2.14 illustrates the derivative of the profiles shown in Fig. 2.13, and it also shows the threshold under which we consider the slope approximately zero. This threshold is set to $0.03K/m$, the accuracy of the thermocouple (Cuxart et al. [2000]). As time progresses, the height increases; at 03:00 LT it is around $26.88m$, while at 05:00 LT it is around $37.55m$. This is only a rough estimate of the height of the SBL. More accurate methods are needed to give a better evaluation.

In Fig. 2.15 is shown a graph of all the wind speed profiles in the time period at the same time. We see that the velocity of the wind doesn't change very much over time, and does not present any particular increase with height (which might indicate the presence of a low level jet). The $R_g \sim 0.1$ at all heights, which suggests that the SBL is in a near neutral stage, well represented by the Monin-Obukhov similarity theory. In this scenario, the turbulence is generated near the ground where the shear is greater, and then transported upward.

2.5.2 Upside-Down Boundary Layer

We defined the SBL as upside-down when the fluxes are increasing with height, therefore when the production of the turbulence is not near the ground but at higher levels and transported downward. As we saw in Section 2.4, the period between 00:00-02:00 LT of the second night (16-September) shows these characteristics. In this section, we are then going to use this time period. In Fig. 2.16, we can see an example of the profiles of the turbulent kinetic energy and of the fluxes of momentum and heat, taken at 01:00 LT. Similarly to Fig. 2.12 we plotted the absolute value of the heat flux for better comparison. The increasing trend of TKE and fluxes with height is appar-

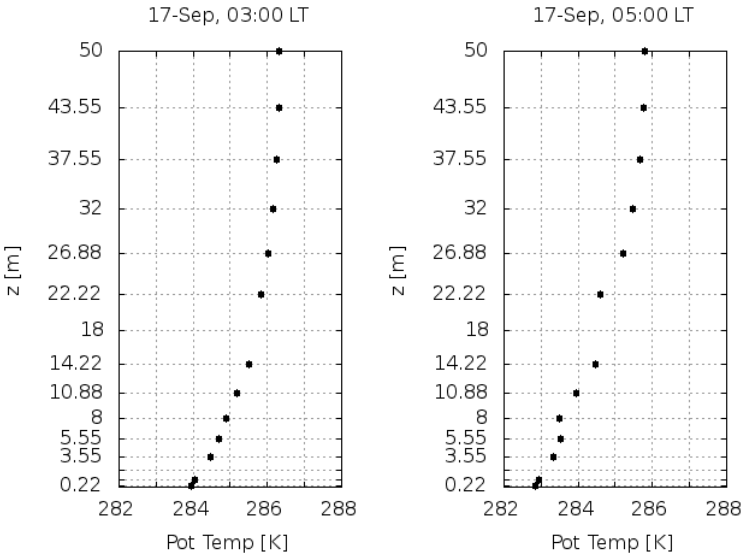

Figure 2.13: *Potential temperature profiles at two different times (03:00 and 05:00 LT).*

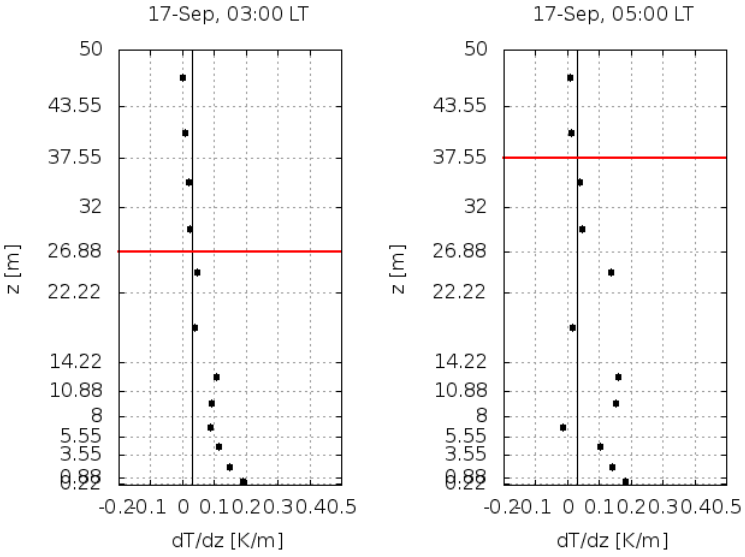

Figure 2.14: *Derivative of the potential temperature profiles represented in Fig. 2.13. The vertical lines indicate the threshold under which the slope is considered zero, while the horizontal lines are the estimate of the temperature height h_t of the SBL.*

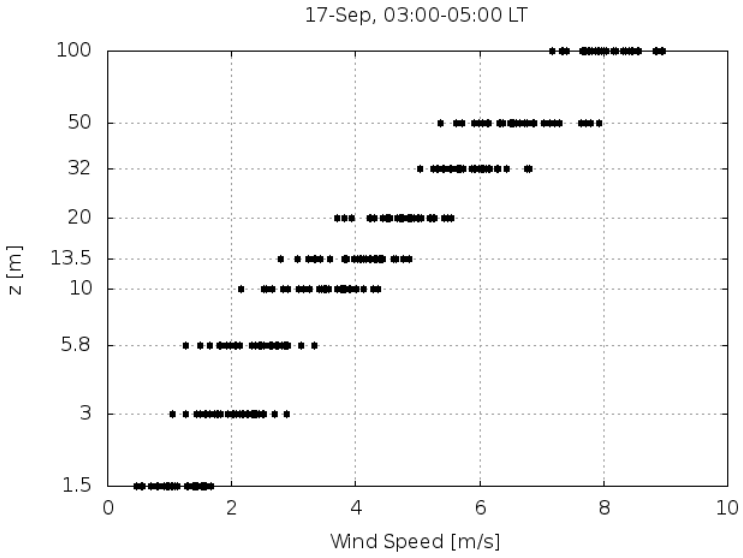

Figure 2.15: *Cumulative wind speed profile showing all the different values of the wind speed over the time period 03:00-05:00 LT, 17-Sep.*

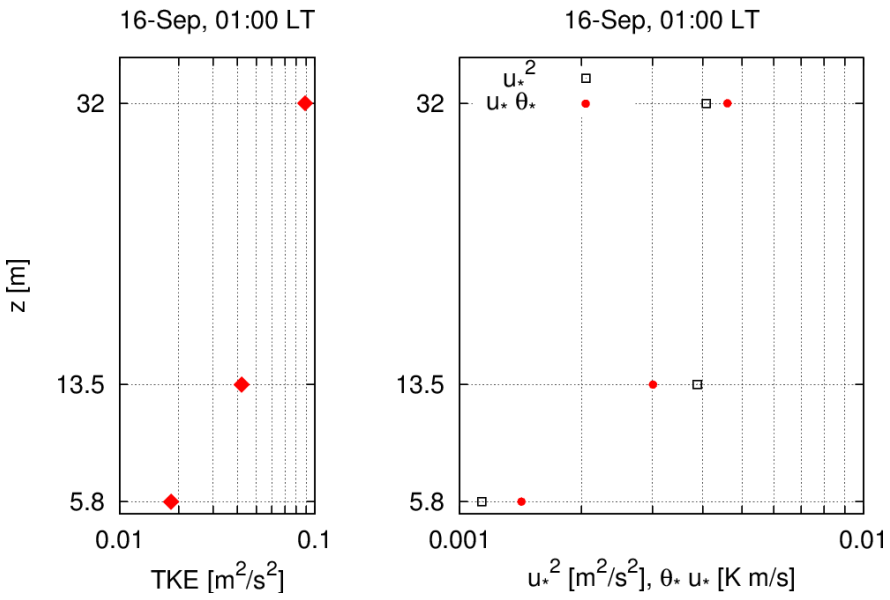

Figure 2.16: *(a) Left panel: profile of the TKE at 01:00 LT, 16-Sep. (b) Right panel: profile of the momentum flux (u_*^2) and the thermal flux ($|\theta_* u_*|$) at 01:00 LT, 16-Sep.*

ent, therefore we can consider this portion of the night as representative of an upside-down boundary layer.

In Fig. 2.17, the wind speed profiles for the time frame considered are shown all together, illustrating a marked increase of the velocities from the ground to the upper layers. It is worth noting that, in the hours before the considered time frame, a strong low level jet developed in the SBL. We can see in Fig. 2.18 that the speed maximum (or *nose*) of the LLJ moved upward with time, from about 32m at 20:30 LT, to 100m at 00:00 LT. Therefore, it is possible to assume that the jet is still present in the time frame considered (from 00:00 LT to 02:00 LT), but at a height above the mast height, outside of the range of the instruments. Its effects are still visible though, because the localized increase of wind speed and shear generates turbulence, which is transported downward by the fluxes, causing the development of the upside-down SBL (Banta et al. [2002], Banta et al. [2003], Banta et al. [2006]).

The potential temperature profiles (Fig. 2.19) show the same characteristic behaviour for the lower layers, with colder ground and warmer atmosphere. Although an increase of θ from a height of approximately $32m$ is noticeable, which can be attributed to the fact that the thermal flux is transporting down the heat from the warm layers above. In this case, since we don't have a real connection to the residual well-mixed layer, it is difficult to define a temperature height of the SBL.

2.6 MultiResolution Flux Decomposition (MRF)

MultiResolution is an orthogonal decomposition algorithm used for computing variances and turbulent fluxes (Howell and Mahrt [1997], Voronovich and Kiely [2007]). In the dataset used in this paper, these parameters were initially calculated from the raw data with a fixed time scale of 300 seconds (referred to as EC data, which stands for Eddie Covariance).

Analyzing the cospectra of these variables, it is possible to identify a gap that separates small-scale turbulence and mesoscale structures. Fitting the cospectra with a 5th-order polynomial, the time scale of the spectral gap is estimated according to a criterion based on the first occurrence of a zero

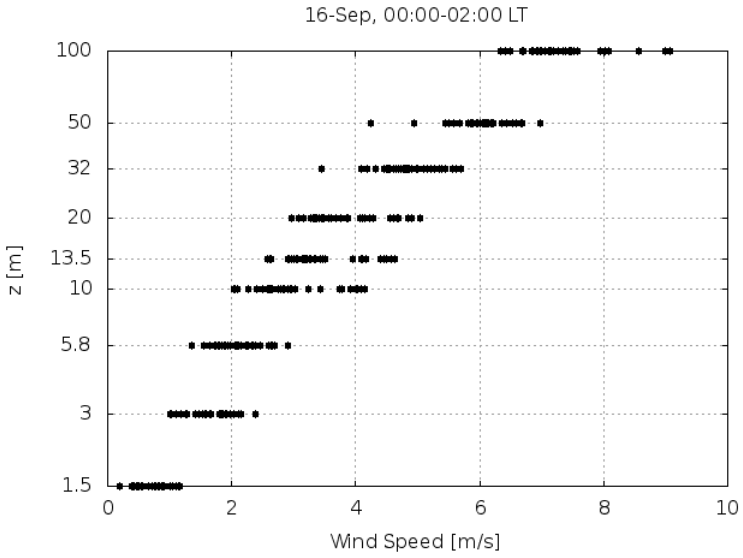

Figure 2.17: *Cumulative wind speed profile showing all the different values of the wind speed over the time period 00:00-02:00 LT, 16-Sep.*

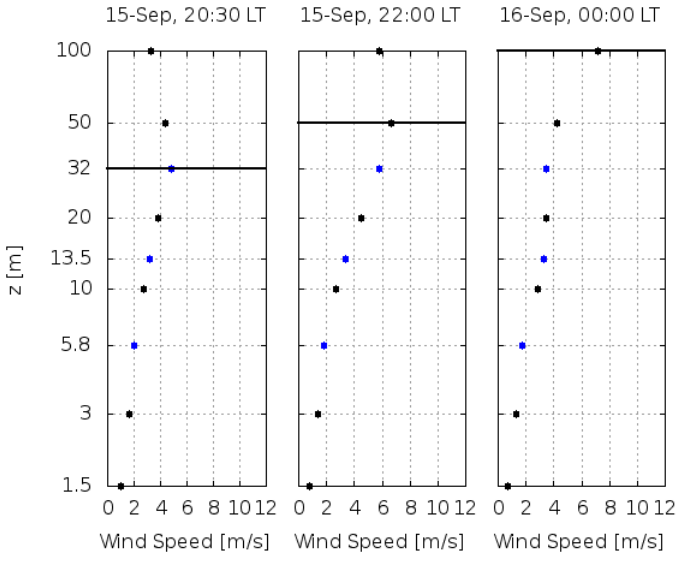

Figure 2.18: *Wind profiles showing the development of a low level jet during the second night of observations at different times.*

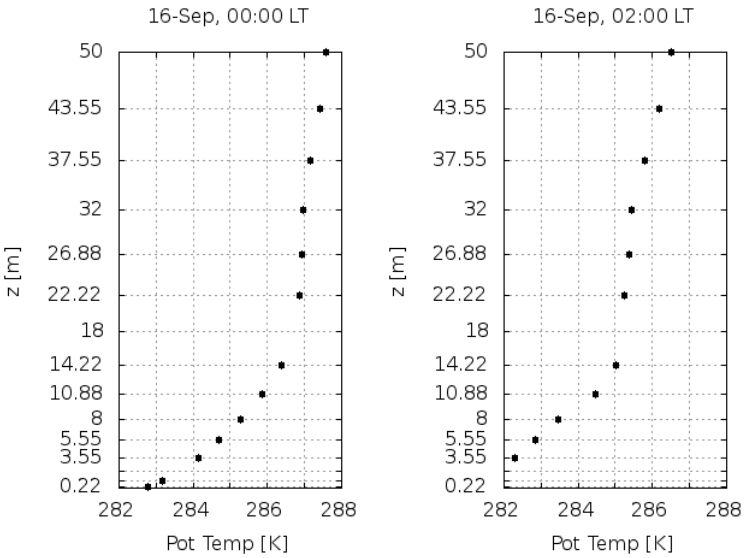

Figure 2.19: *Potential temperature profiles at two different times (00:00 and 02:00 Local Time).*

crossing or inflection point after the maximum value. This new time scale is then used to re-calculate variances (σ_w, σ_θ), turbulent fluxes (u_*, θ_*) and the Monin-Obukhov length L_{MO} (which depends on the fluxes), referred to henceforth as *MRF data*.

To compare the two sets of data (e.g. for the u_*), we evaluated the percentual relative differences

$$\Delta_r^{\%} = \frac{|u_*^{EC} - u_*^{MRF}|}{u_*^{EC}}$$

In Fig. 2.20 are shown the time series of these errors for the second night (15-16 Sep) and the third night (16-17 Sep), and we can see that the errors are sometimes very large, even reaching 100%. This does not mean that this information is wrong or that the procedure is incorrect. Rather, it illustrates that the process of cutting part of the spectrum is eliminating processes at scales bigger than the turbulence, which we do not need to analyze.

In Fig. 2.21 is shown how $\Delta_r^{\%}$ varies with stability, using the gradient Richardson number R_g. It is possible to see that the errors increase with increasing R_g. In fact, in stable conditions (considered for $R_g \simeq 0.1$), the

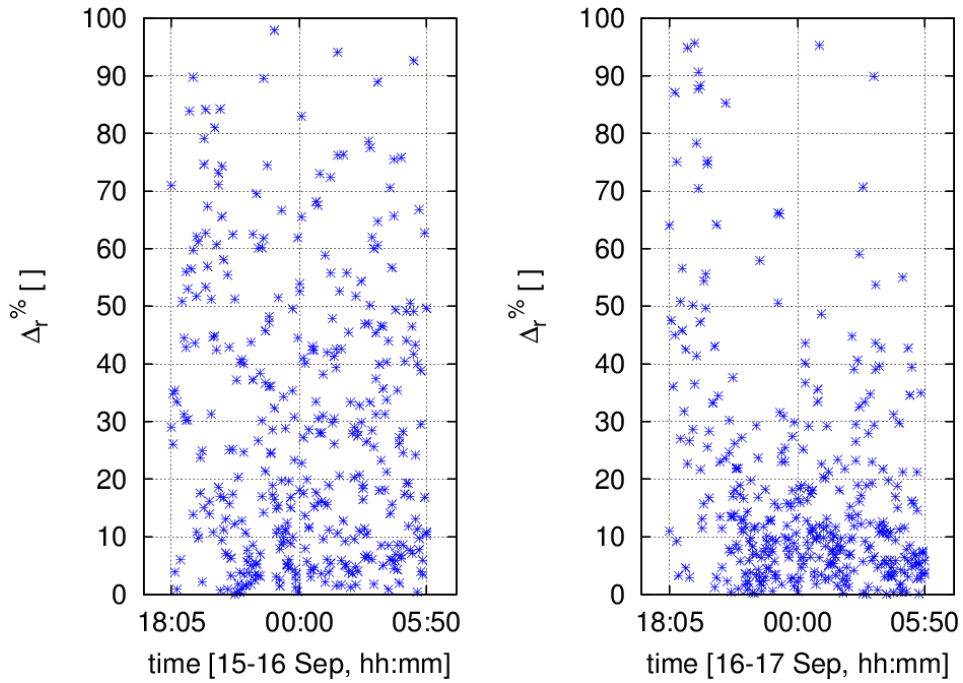

Figure 2.20: *Time series of $\Delta_r^{\%}$ during the second (left panel) and third (right panel) nights of the experiment.*

fluxes are very small, which increase the errors due to the small sensitivity of the instruments. This behaviour is also visible in Fig. 2.22, where we plotted $\Delta_r^{\%}$ as a function of u_*^{MRF}. The accuracy of the cup anemometers is $0.2m/s$ (Cuxart et al. [2000]), and the order of magnitude of the ratio u/u_* at $R_g \simeq 0.1$ is approximately 10 (evaluated later in this study). This means that the accuracy of u_* can be taken of the order of 0.02. This value is in agreement with Fig. 2.22, which shows an increase of the relative error for values of u_* smaller than the accuracy.

In the rest of this study, where not otherwise specified, we are going to use only the MRF set of variables, considered more representative of the turbulence.

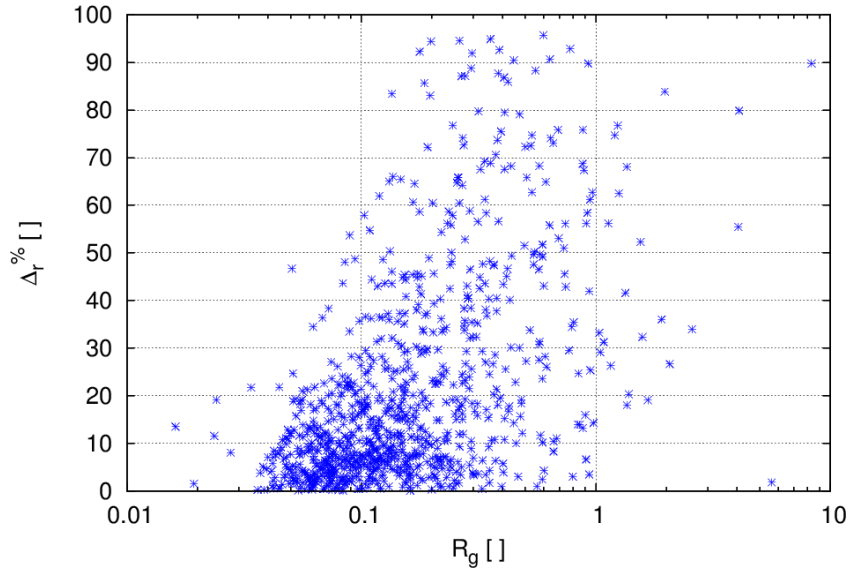

Figure 2.21: *The variation of* $\Delta_r^{\%}$ *with stability using* R_g.

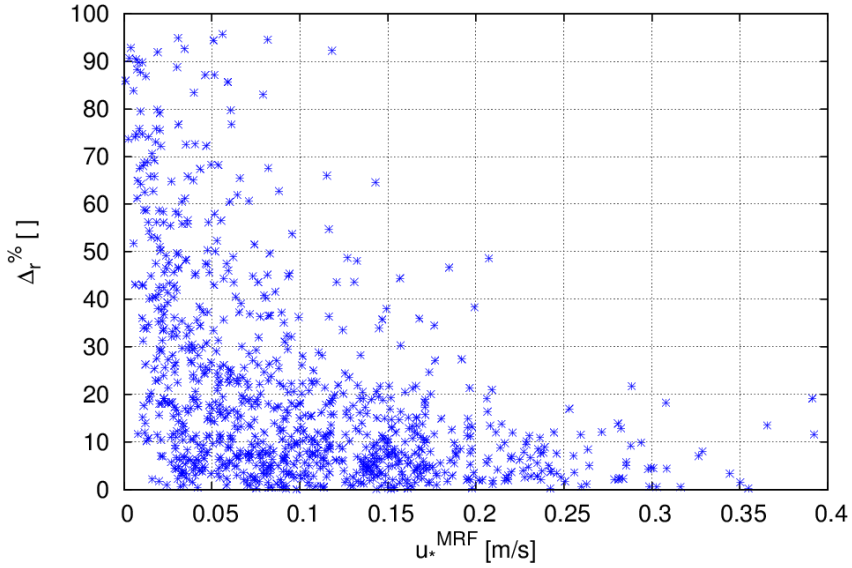

Figure 2.22: *The variation of* $\Delta_r^{\%}$ *with* u_*^{MRF}.

2.7 Personal Case Selection

2.7.1 Wind Threshold

As we saw in the previous section, we used the MR decomposition in order to separate the contributions of the turbulence and of the mesoscale processes from the variances and fluxes cospectra. For example, we can see in Fig. 2.23 a scatter plot of $\zeta = z/L_{MO}$ evaluated with the two different methods (EC and MRF) at a height of $5.8m$. It is possible to see that the data points are mostly around the bisector $\zeta_{EC} = \zeta_{MRF}$, but that some of them are quite scattered. In this section, we are trying to find a way to reduce this scatter, therefore the points that will remain after the removal will be the most representative of the turbulence. We used as a parameter the wind speed between $0m/s$ and $8m/s$, with intervals of $0.05m/s$, and for each speed v_i, we defined the function:

$$\delta(v_i) = \sum_{\forall t} |\zeta_{EC} - \zeta_{MRF}| \qquad \forall v < v_i \tag{2.3}$$

We then plotted the normalized functions with respect to the velocity (Fig. 2.24). We can see that, with increasing speeds, the differences between EC and MRF data are decreasing. We defined as not significantly scattered the data with a normalized $\delta \leq 0.2$, therefore we need to estimate the correspondent velocity for each height. To fit the data, we used a function as follows (B,C parameters of the fit):

$$Fit\left(\delta(v)\right) = \left(1 + e^{\frac{v-B}{C}}\right)^{-1}$$

which allowed us to determine the wind speed limit for each height ($2.1m/s$ at $5.8m$, $3.6m/s$ at $13.5m$ and $5.5m/s$ at $32m$).

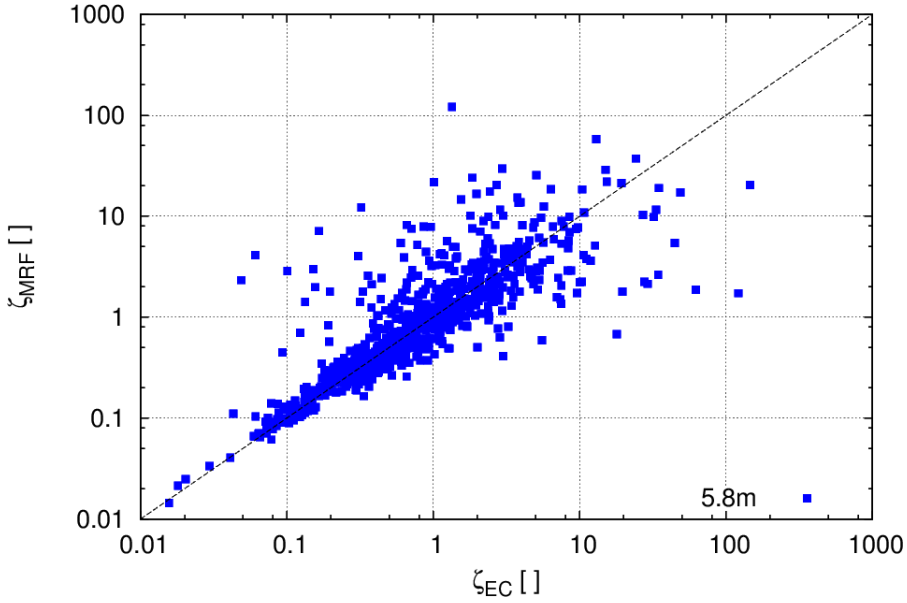

Figure 2.23: *Scatter plot of $\zeta(5.8m)$, calculated with EC and MRF methods.*

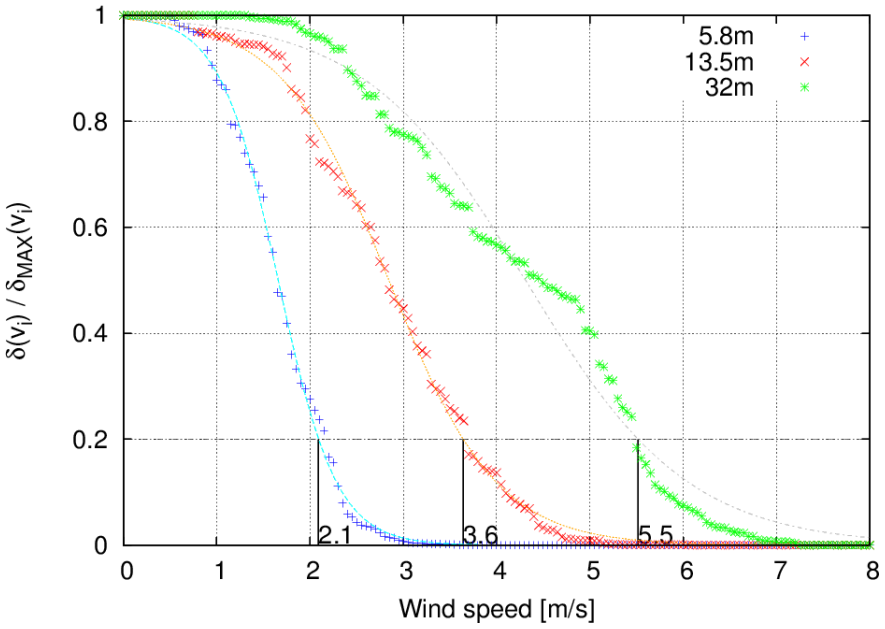

Figure 2.24: *Normalized $\delta(v)$ and correspondent fits functions at $5.8m$, $13.5m$ and $32m$.*

2.7.2 Anisotropy

Fig. 2.25 shows the variation of the wind speed (at $5.8m$) with the gradient Richardson number R_g calculated at the same height, and we can observe that the wind speed decreases as the SBL becomes more stable.

Turbulence in the SBL is produced by wind shear and destroyed by buoyancy effects (and viscous dissipation). As the stratification becomes stronger, the vertical turbulence exchange is dampened, leading to the development of strong spatial anisotropy. Turbulence anisotropy is defined as the ratio of the vertical and horizontal turbulent velocity variances (Luhar et al. [2009]) as expressed by the following formula:

$$Anisotropy = \frac{\sigma_w^2}{\sigma_u^2 + \sigma_v^2} \tag{2.4}$$

In Fig. 2.26 is shown the turbulence anisotropy as a function of different stability parameters (ζ, R_g and R_b, the last one calculated using data measured at 3m and 10m). We can see that, with increasing stability, the anisotropy becomes stronger. Considering the bulk Richardson numbers, we calculated the average anisotropy for intervals of R_b of $10^{0.1}$, and then we tried to fit these averaged data with the following function (B,C parameters of the fit):

$$Fit(\overline{Anisotropy}) = \left(1 + e^{\frac{v-B}{C}}\right)^{-1}$$

We then evaluated the bulk Richardson number that separates the two stability regimes as the value at which the fit function reaches 95% of its initial value, finding $R_b \simeq 0.163$ (Fig. 2.27).

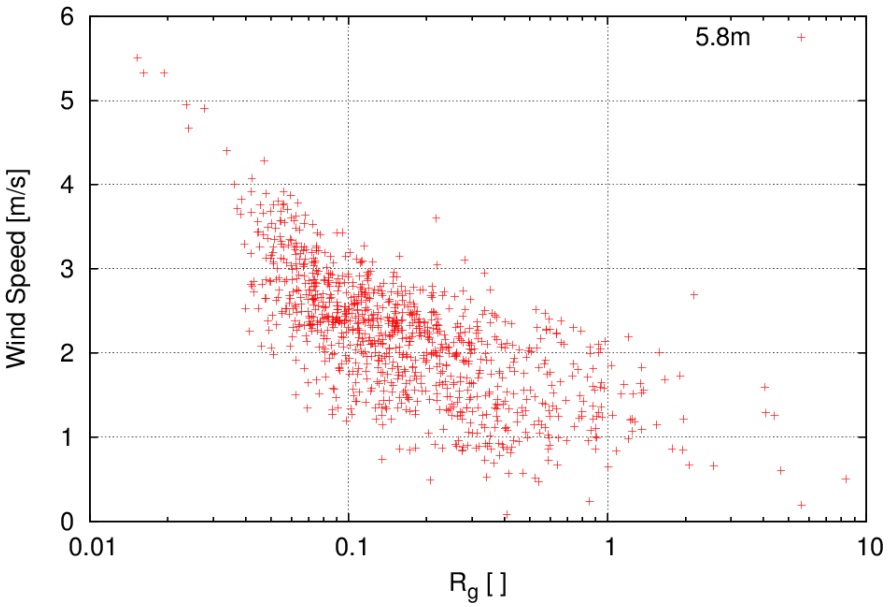

Figure 2.25: *Scatter plot of wind speed at 5.8m versus R_g.*

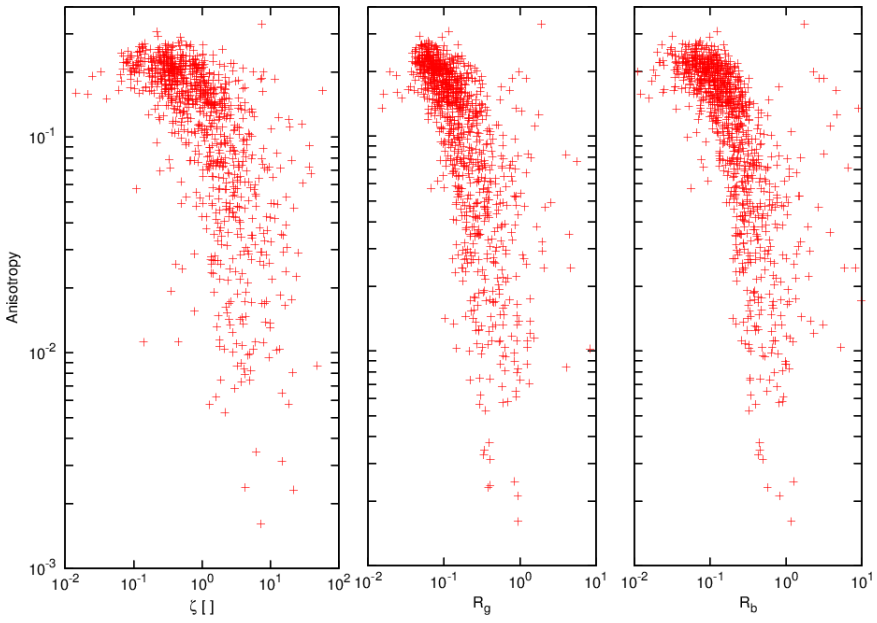

Figure 2.26: *Variation of anisotropy with (a) the stability parameter ζ, (b) gradient Richardson number R_g and (c) bulk Richardson number R_b.*

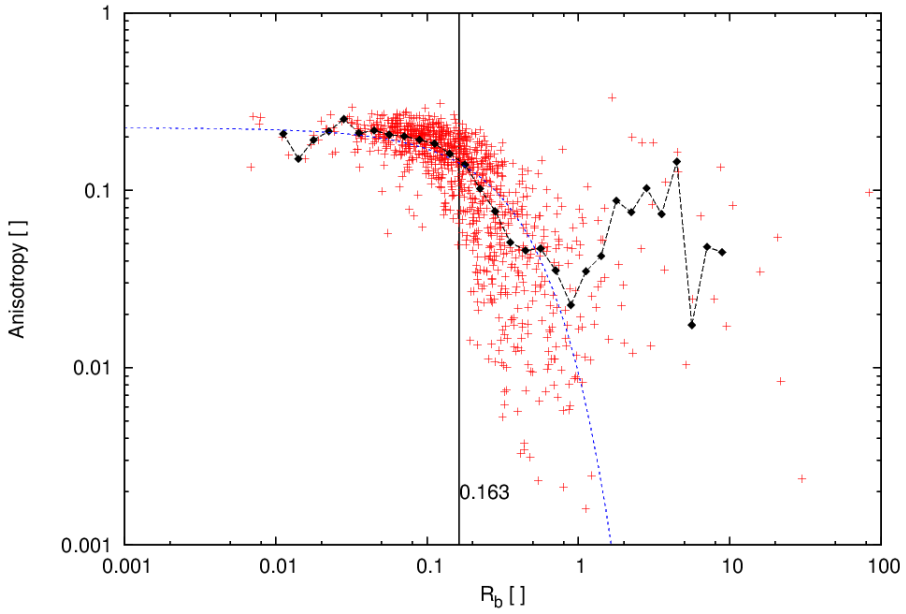

Figure 2.27: *Variation of anisotropy with the bulk Richardson number, fit function and Threshold value for* R_b.

2.7.3 New Classification of Cases

In the previous section, we were able to define different thresholds in wind speed at different heights (5.8m, 13.5m and 32m) and in stability parameters (R_g or R_b). In the first case, we defined that, for winds stronger than a certain speed limit ($u_t(5.8m) = 2.1m/s$, $u_t(13.5m) = 3.6m/s$ and $u_t(32m) = 5.5m/s$), the turbulence in the SBL is better represented due to the cut in the cospectra of the turbulent fluxes and variances. Furthermore, we noticed that high winds are connected to weaker stability, and we found a threshold for the stability parameters $R_g \simeq R_b = 0.163$ analyzing the behaviour of the anisotropy of the turbulence.

We are going to use these two parameters (wind speed and stability) to define a different set of cases, which are intended to represent the turbulence of the SBL in a better way. In particular, the case that we are most interested in is the one defined by strong wind speed ($u > u_t$ dependent on the height) and weak stability ($R_g < 0.163$).

Chapter 3

Similarity Theories

3.1 Local MOST

Monin-Obukhov similarity theory (MOST) for the PBL was developed for a stationary atmospheric surface layer over horizontally homogeneous terrain. As we saw in Chapter 1.6.2, the structure of the turbulence is determined by the kinematic stress τ_0/ρ, the heat flux $\overline{w'\theta'}|_0$, the buoyancy parameter β and the height above the ground z (Pahlow et al. [2001]), where the fluxes are calculated at ground level. These parameters are necessary to define the different scales for velocity (u_*), temperature (θ_*) and length (L_{MO}), chosen as surface-layer scales.

In near-neutral conditions, the K-theory determined that the natural length scale in a turbulent boundary layer is the distance z from the surface (Tennekes and Lumley [1972],Mahrt et al. [1979], Caughey et al. [1979]). Loosely speaking, the largest eddies at height z would have a size limited only by the distance to the surface itself.

As stability increases, however, the effect of the turbulence is to limit vertical movements, consequently turbulent eddies cannot extend across the whole boundary layer anymore. Therefore, the distance to the surface ceases to play any role in the structure of the turbulence, which becomes decoupled with the surface fluxes and acts in relation to the fluxes at the same height (Nieuwstadt [1984], Dias et al. [1995], Yagüe et al. [2006]).

This is called *local Monin-Obukhov similarity theory*, and we are going to use it throughout the rest of this study. The Monin-Obukhov length is now evaluated with the local fluxes and called Λ_{MO}.

3.2 Similarity Functions

3.2.1 Equations

In this section we are going to list the different universal similarity functions $\phi_m(\zeta)$, $\phi_h(\zeta)$ and the universal relative similarity functions $\psi(\zeta, \zeta_{0m})$, $\psi(\zeta, \zeta_{0h})$ that we are going to use, formulated from four different authors.

Since we are using local MOST, $\zeta = z/\Lambda_{MO}$, $\zeta_{0m} = z_{0m}/\Lambda_{MO}$ and $\zeta_{0h} = z_{0h}/\Lambda_{MO}$.

- Högström [1996], (from now on referred as $H96$), with $\alpha_{m3} = 6.0$, $\alpha_{h0} = 0.95$, $\alpha_{h2} = 7.99$:

$$\phi_m^{H96}(\zeta) = 1 + \alpha_{m3}\zeta, \tag{3.1a}$$

$$\phi_h^{H96}(\zeta) = \alpha_{h0} + \alpha_{h2}\zeta, \tag{3.1b}$$

$$\Psi_m^{H96}(\zeta, \zeta_{0m}) = \alpha_{m3}(\zeta - \zeta_{0m}), \tag{3.1c}$$

$$\Psi_h^{H96}(\zeta, \zeta_{0h}) = (\alpha_{h0} - 1)\, ln\left(\frac{\zeta}{\zeta_{0h}}\right) + \alpha_{h2}(\zeta - \zeta_{0h}) \tag{3.1d}$$

- Webb [1970], (from now on referred as $W70$), with $\beta_1 = 4.2$, $\alpha = 0.95$, $\beta_2 = 7.03$:

$$\phi_m^{W70}(\zeta) = 1 + \beta_1\zeta, \tag{3.2a}$$

$$\phi_h^{W70}(\zeta) = \alpha + \beta_2\zeta, \tag{3.2b}$$

$$\Psi_m^{W70}(\zeta, \zeta_{0m}) = \beta_1(\zeta - \zeta_{0m}), \tag{3.2c}$$

$$\Psi_h^{W70}(\zeta, \zeta_{0h}) = (\alpha - 1)\, ln\left(\frac{\zeta}{\zeta_{0h}}\right) + \beta_2(\zeta - \zeta_{0h}) \tag{3.2d}$$

- Cheng and Brutsaert [2005], (from now on referred as $CB05$), with $a = 6.1$, $b = 2.5$, $c = 5.3$, $d = 1.1$:

$$\phi_m^{CB05}(\zeta) = 1 + a\left(\frac{\zeta + \zeta^b(1+\zeta^b)^{\frac{1-b}{b}}}{\zeta + (1+\zeta^b)^{\frac{1}{b}}}\right), \tag{3.3a}$$

$$\phi_h^{CB05}(\zeta) = 1 + c\left(\frac{\zeta + \zeta^d(1+\zeta^d)^{\frac{1-d}{d}}}{\zeta + (1+\zeta^d)^{\frac{1}{d}}}\right), \tag{3.3b}$$

$$\Psi_m^{CB05}(\zeta, \zeta_{0m}) = a \cdot ln\left(\frac{\zeta + (1+\zeta^b)^{\frac{1}{b}}}{\zeta_{0m} + (1+\zeta_{0m}^b)^{\frac{1}{b}}}\right), \tag{3.3c}$$

$$\Psi_h^{CB05}(\zeta, \zeta_{0h}) = c \cdot ln\left(\frac{\zeta + (1+\zeta^d)^{\frac{1}{d}}}{\zeta_{0h} + (1+\zeta_{0h}^d)^{\frac{1}{d}}}\right) \tag{3.3d}$$

- Beljaars and Holtslag [1991], (from now on referred as $BH91$), with $a = 0.7$, $b = 0.667$, $c = 5.0$, $d = 0.35$:

$$\phi_m^{BH91}(\zeta) = 1 + a\zeta + b\zeta(1 + c - d\zeta)e^{-d\zeta}, \tag{3.4a}$$

$$\phi_h^{BH91}(\zeta) = 1 + a\zeta(1 + ab\zeta) + b\zeta(1 + c - d\zeta)e^{-d\zeta}, \tag{3.4b}$$

$$\begin{aligned}\Psi_m^{BH91}(\zeta, \zeta_{0h}) = {} & a(\zeta - \zeta_{0m}) + \\ & + b\left[(\zeta - \frac{c}{d})e^{-d\zeta} - (\zeta_{0m} - \frac{c}{d})e^{-d\zeta_{0m}}\right],\end{aligned} \tag{3.4c}$$

$$\begin{aligned}\Psi_h^{BH91}(\zeta, \zeta_{0m}) = {} & (1 + ab\zeta)^{\frac{1}{b}} + b(\zeta - \frac{c}{d})e^{-d\zeta} + \\ & - (1 + ab\zeta_{0h})^{\frac{1}{b}} - b(\zeta_{0h} - \frac{c}{d})e^{-d\zeta_{0h}}\end{aligned} \tag{3.4d}$$

3.2.2 Similarity Functions for Wind

The relationship between $\Upsilon_m(\zeta, \zeta_{0m})$ and Λ_{MO}^{-1} can be seen in Fig. 3.1 for the three height studied (5.8m, 13.5m and 32m). As we defined in Eq. 1.43, we plotted:

$$\kappa \frac{\overline{u}(z)}{u_*(z)} = \Upsilon_m(\zeta, \zeta_{0m}) = ln\left(\frac{z}{z_{0m}}\right) + \Psi_m(\zeta, \zeta_{0m}) \tag{3.5}$$

where $\kappa = 0.4$, $z_{0m} = 0.049m$, $\overline{u}(z)$ and $u_*(z)$ are taken from the dataset, and we defined the different $\Psi_m(\zeta, \zeta_{0m})$ functions for different authors in the previous section (Eqs. 3.1c, 3.2c, 3.3c and 3.4c). The value of the scale coefficient between $u(z)$ and $u_*(z)$ in near neutral conditions ($\Lambda_{MO}^{-1} \to 0$) is in average $u/u_* \simeq 15$, for the different heights.

It is possible to observe that the data points are more scattered as the height increases, especially for lower stability. The vertical lines plotted in Fig. 3.1 are at $\Lambda_{MO}^{-1} = 1/z$, where z is the considered height for each graph. This represents the separation between the region of the SBL dominated by mechanical turbulence and the one dominated by thermal turbulence, respectively below and above this value. As height increases, the wind shear (therefore the momentum flux) decreases, so the heat flux is more efficient in damping the turbulent eddies, increasing the stability of the SBL.

Another consequence of this behavior is that, while the considered similarity functions seem to well represent the data for low stability, for high values of Λ_{MO}^{-1} the data are overestimated, and they appear to level off. This is particularly noticeable in the third graph (at $z = 32m$). The high stratification in this layer inhibits vertical motion and tends to reduce the size of the turbulent eddies. When their length scale becomes smaller than the height above the ground, turbulence doesn't feel the presence of the surface (it is decoupled from it), and an explicit dependence on z disappears. This behavior is often referred as *z-less stratification* (Dias et al. [1995], Klipp and Mahrt [2004]).

In Fig. 3.2 we plotted the similarity functions $\Upsilon_m(\zeta, \zeta_{0m})$, this time separating the cases 1 and 4 (when the momentum fluxes are monotonically increasing or decreasing with height), as we defined in Chapter 2.3. We can

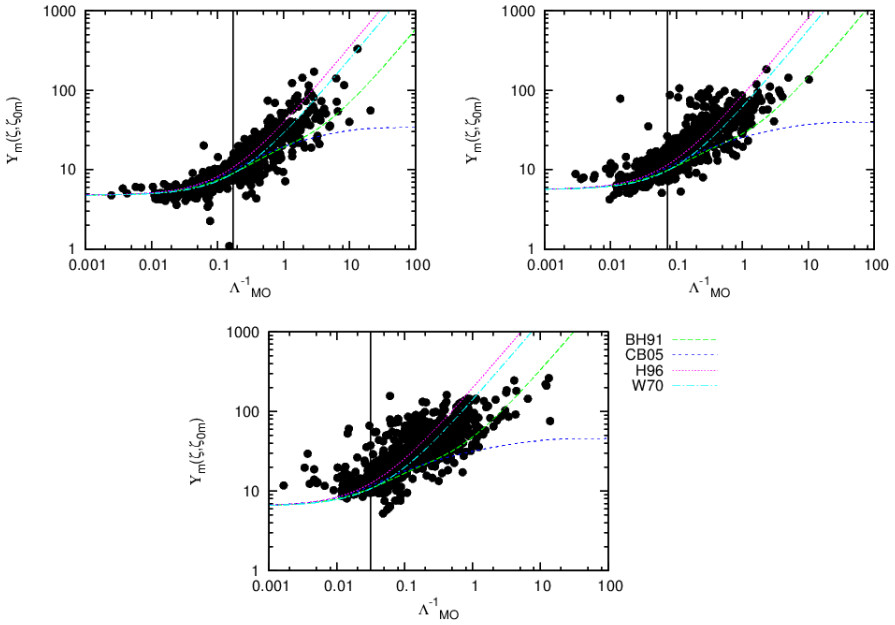

Figure 3.1: $\Upsilon_m(\zeta, \zeta_{0m})$ *versus* Λ_{MO}^{-1} *for all the data in the dataset at: (a) 5.8m, (b) 13.5m and (c) 32m. Similarity functions found by different authors are also shown for comparison.*

notice that the two cases are well separated only at the lower level ($5.8m$), while at higher levels the data points are mixed together. This is because the instruments at $z = 5.8m$ are within the surface layer, where the influence of the ground is great, and the turbulence generated is transported upwards (the condition for a *traditional SBL*). At higher levels, the stability increases and the turbulence is produced locally, therefore the increase or decrease of the fluxes with height does not strongly depend on what happens on the surface.

In Fig. 3.3 we followed the same procedure as for the previous set of figures, but this time separating the data with the new classification of the cases using the wind speed and the gradient Richardson number, as we defined in Chapter 2.7. In this analysis, it is possible to see that the data with strong winds and weak stability are very well represented by the similarity functions at every height and with very low scatter.

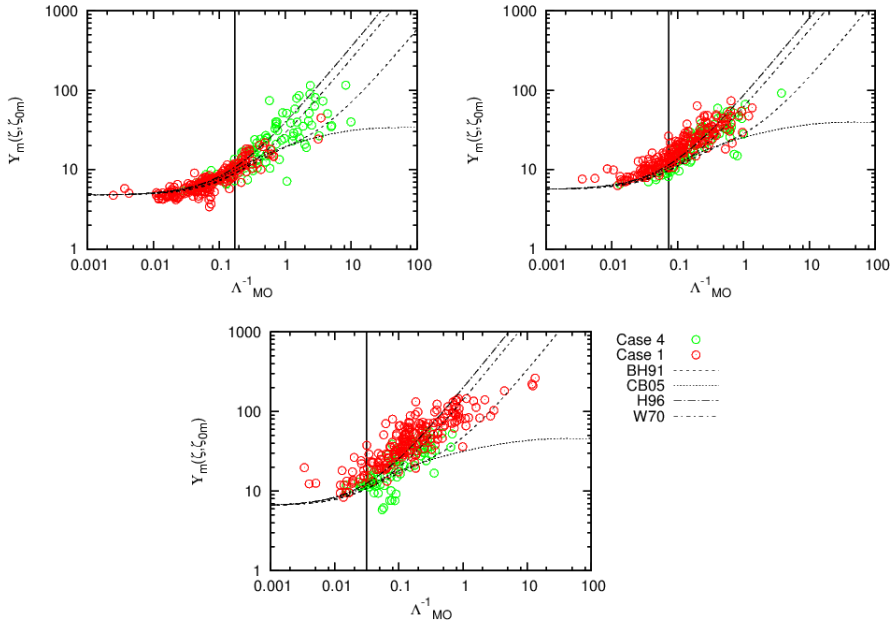

Figure 3.2: *Like Fig. 3.1, separating Case=1,4.*

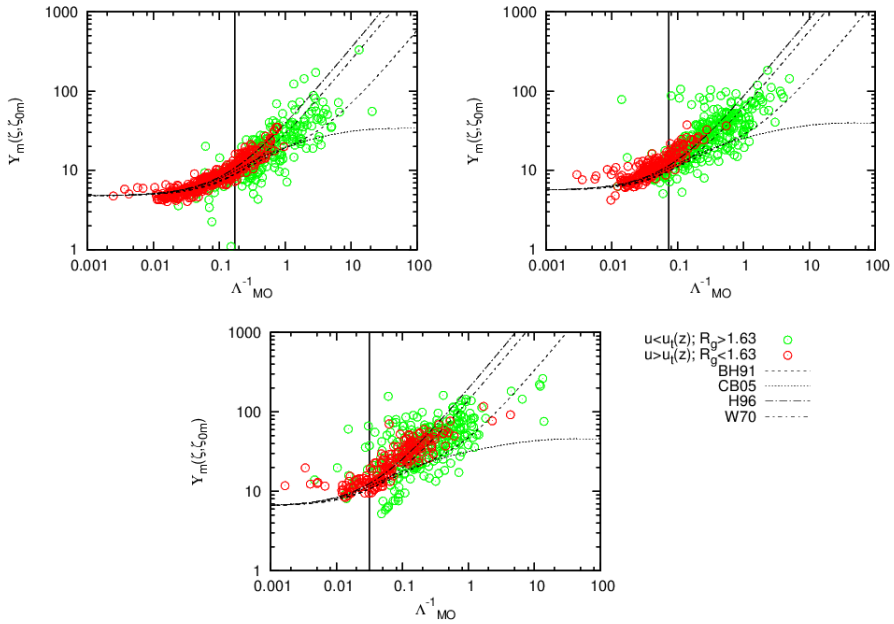

Figure 3.3: *Like Fig. 3.1, separating cases where* $u > u_t(z), R_g < 0.163$ *and cases where* $u < u_t(z), R_g > 0.163$. *The different values of* $u_t(z)$ *were defined in Chapter 2.7.*

3.2.3 Similarity Functions for Temperature

In Fig. 3.4 we represented the relationship between $\Upsilon_m(\zeta, \zeta_{0m})$ and Λ_{MO}^{-1}. As we defined in Eq. 1.46, we plotted:

$$-\kappa \frac{\theta(z) - \theta(z_{0h})}{\theta_*} = \Upsilon_h(\zeta, \zeta_0) = ln\left(\frac{z}{z_{0h}}\right) + \Psi_h(\zeta, \zeta_{0h}) \tag{3.6}$$

where $\kappa = 0.4$, $z_{0h} = 3 \cdot 10^{-4} m$, $\theta(z)$, $\theta(z_{0h})$ and $\theta_*(z)$ are taken from the dataset, and we defined the different $\Psi_h(\zeta, \zeta_{0h})$ functions for different authors in the previous section (Eqs. 3.1d, 3.2d, 3.3d and 3.4d). The data for the temperatures were not taken at the same heights as the Λ_{MO}^{-1}, therefore we used different levels for the $\theta(z)$, $5.55m$, $14.22m$ and $32m$.

As Fig. 3.4 shows, the results are much more scattered then those for Υ_m, which could be attributed to lower accuracy in the measurements, or to the fact that turbulent scaling laws assume stationary situations, but the SBL is frequently non-stationary due to intermittent turbulence (Klipp and Mahrt [2004], Mahrt [2007], Mahrt [2011], Coulter and Doran [2002]).

In Fig. 3.5 we plotted the similarity functions $\Upsilon_h(\zeta, \zeta_{0h})$, this time separating the cases 1 and 4 (when the heat fluxes are monotonically increasing or decreasing with height), as we defined in Chapter 2.3. As for the wind similarity function, we plotted vertical lines in this figure at $\Lambda_{MO}^{-1} = 1/z$, where z is the considered height for each graph. We can see that the scatter increases in the region dominated by the thermal fluxes, where $\Lambda_{MO}^{-1} > 1/z$. The scatter for the higher levels ($14.22m$ and $32m$) is very high, and cases 1 and 4 are not easily distinguishable. Otherwise, at the lower level ($5.55m$), data for case 1 follows the similarity functions with reasonable agreement.

In Fig. 3.6 we plotted the $\Upsilon_h(\zeta, \zeta_{0h})$, separating the data using the new classification of the cases based on wind speed and gradient Richardson number, as we defined in Chapter 2.7. The scatter is still present at every level (especially at $32m$), but we can see a better agreement with the similarity functions for strong winds and weak stability.

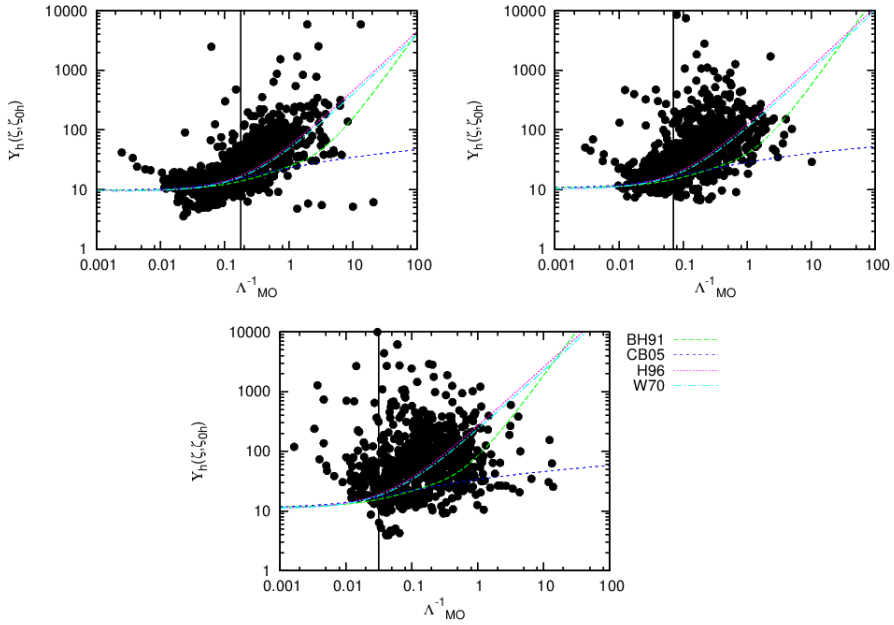

Figure 3.4: $\Upsilon_h(\zeta, \zeta_{0h})$ *versus* Λ_{MO}^{-1} *for all the data in the dataset at: (a) 5.8m, (b) 13.5m and (c) 32m. Similarity functions found by different authors are also shown for comparison.*

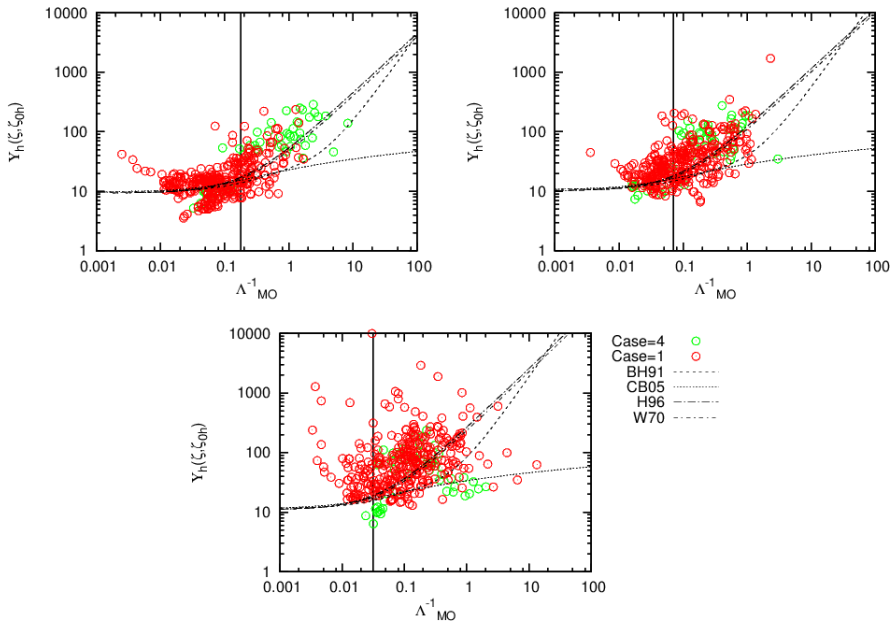

Figure 3.5: *Like Fig. 3.4, separating Case=1,4.*

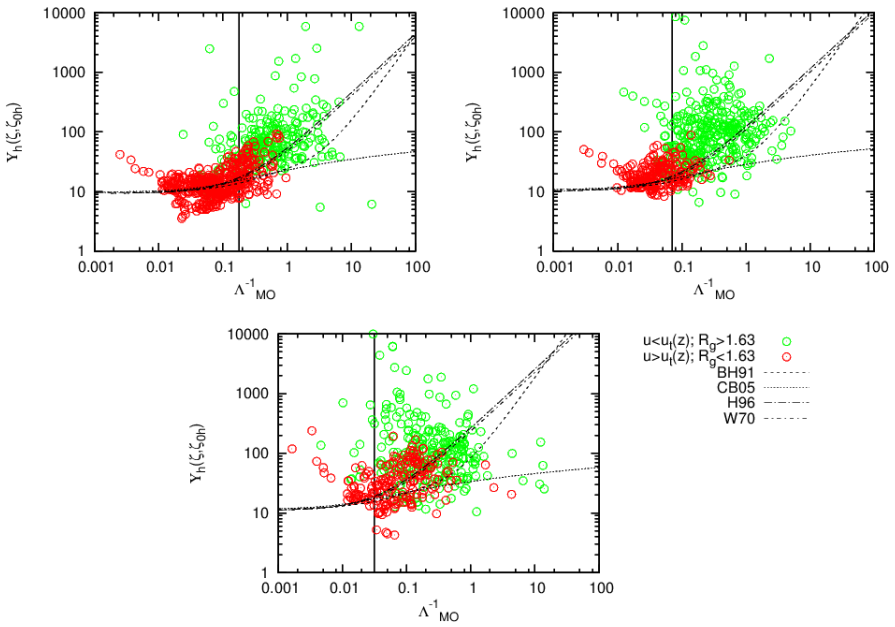

Figure 3.6: *Like Fig. 3.4, separating cases where* $u > u_t(z), R_g < 0.163$ *and cases where* $u < u_t(z), R_g > 0.163$. *The different values of* $u_t(z)$ *were defined in Chapter 2.7.*

3.2.4 Eliminating the Dependence on z_0

As we saw in the previous section, the similarity functions depend on the surface roughness length for wind z_{0m} and for temperature z_{0h}. These two parameters have been determined by extrapolation of the data in near-neutral condition, therefore they are greatly affected by the errors in the data.

In this section, we are going to eliminate the dependence on these variables, in order to reduce the scatter due to experimental errors. This method consists of evaluating the difference between wind speed (or potential temperature) at two specific heights, therefore all the terms in the equations that depend on z_0 will cancel out. It is worth noting that, in Eqs. 3.5 and 3.6, the scale variables (u_* and θ_*) are evaluated at the height where the measurements are taken. This means that, in the following equations, since we have two different heights, the value of these scale variables needs to be representative of the layer analyzed. For wind speed, we took $z_1 = 13.5m$, $z_2 = 5.8m$ and evaluated $u_* = (u_*(z_1) + u_*(z_2))/2$. For potential temperature

we considered $z_1 = 10.88m$, $z_2 = 0.88m$ and $\theta_* = \theta_*(5.8m)$.

The similarity equations for the differences of wind speed and potential temperature are listed here, where $\zeta_1 = z_1/\Lambda_{MO}$ and $\zeta_2 = z_2/\Lambda_{MO}$.

$$\kappa \frac{\overline{u}(z_1) - \overline{u}(z_2)}{u_*} = \Upsilon_m(\zeta_1, \zeta_2) = ln\left(\frac{z_1}{z_2}\right) + \Psi_m(\zeta_1, \zeta_{0m}) - \Psi_m(\zeta_2, \zeta_{0m}) \quad (3.7)$$

$$-\kappa \frac{\theta(z_1) - \theta(z_2)}{\theta_*} = \Upsilon_h(\zeta_1, \zeta_2) = ln\left(\frac{z_1}{z_2}\right) + \Psi_h(\zeta_1, \zeta_{0h}) - \Psi_h(\zeta_2, \zeta_{0h}) \quad (3.8)$$

In Figs. 3.7 and 3.8 we plotted the similarity functions $\Upsilon_m(\zeta_1, \zeta_2)$ and $\Upsilon_h(\zeta_1, \zeta_2)$ for all data (top-left panel), separating the cases 1 and 4 (top-right panel) and separating the cases with the new classification based on wind speed and gradient Richardson number (bottom panel).

For both wind speed and potential temperature, we notice that the scatter has been greatly reduced. Data for case 1 and for $u > 2.1m/s$, $R_g < 0.163$ (i.e. data of traditional SBL) are well represented by the similarity functions. For the wind speed this data seems to follow the linear functions ($H96$ and $W70$) even for stronger stability, although the same cannot be said for the potential temperature.

3.2.5 Richardson Numbers

We described in Chapter 1.6.5 the relationships between the different Richardson numbers and the stability parameter ζ, using the various similarity functions $\phi(\zeta)$ and $\Upsilon(\zeta, \zeta_0)$.

In Fig. 3.9 we can see the behaviour of the Richardson numbers at z=5.8m, and the analytic functions described in Eqs. 1.47, 1.49 and 1.50 using similarity functions found by different authors. The values for R_f and R_g can be directly found in the dataset, while R_b has to be evaluated between different levels. We used $z_1 = 8.0m, z_2 = 3.55m$ as levels for the temperature, and $z_3 = 10.0m, z_4 = 3.0m$ for the wind speed, taking $z = 5.8m$ as reference height to evaluate the fluxes.

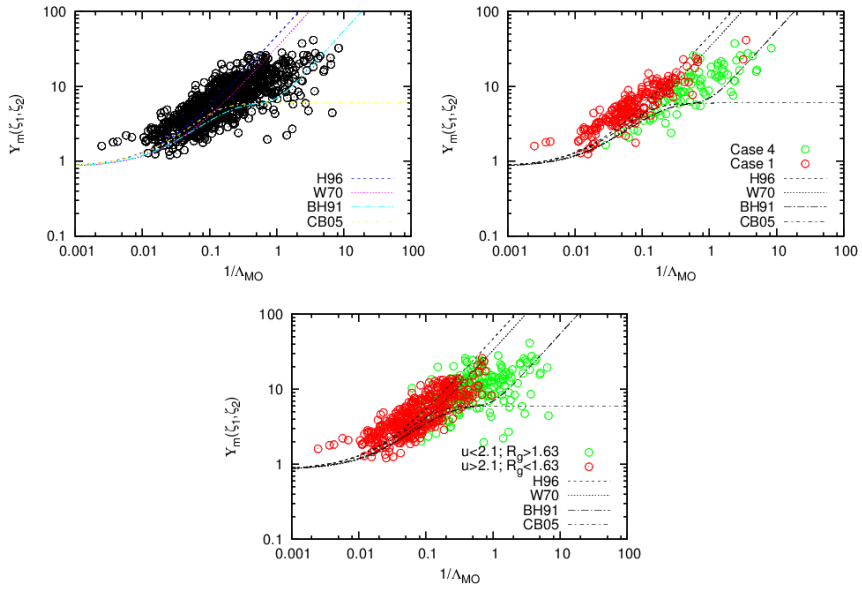

Figure 3.7: $\Upsilon_m(\zeta_1, \zeta_2)$ *versus* Λ_{MO}^{-1} *for all the data in the dataset. Wind speeds are calculated at* $z_1 = 13.5m$ *and* $z_2 = 5.8m$*, and* u_* *is evaluated averaging* $u_*(5.8)$ *and* $u_*(13.5)$*. Similarity functions found by different authors are also shown for comparison.*

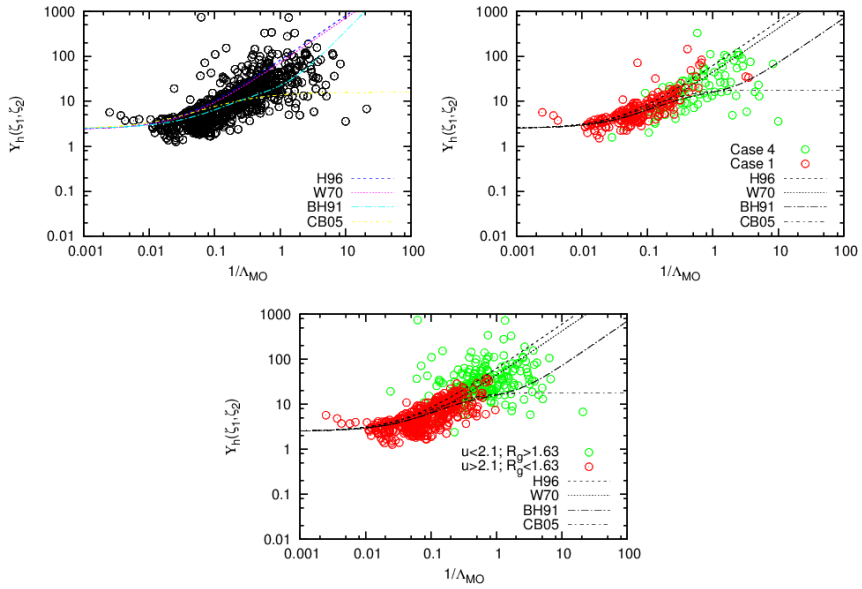

Figure 3.8: $\Upsilon_h(\zeta_1, \zeta_2)$ *versus* Λ_{MO}^{-1} *for all the data in the dataset. Potential temperatures are calculated at* $z_1 = 10.88m$ *and* $z_2 = 0.88m$*, and* θ_* *is evaluated at* $5.8m$*. Similarity functions found by different authors are also shown for comparison.*

The gradient Richardson number is a widely used stability parameter relating thermal stratification to wind shear (Yagüe et al. [2006]). When relationships between turbulent and stability parameters are studied, one problem is self-correlation, i.e. the parameters share one or more variables. In our case, one example is that both ϕ_m and ζ contain u_*. This feature was analyzed by Klipp and Mahrt [2004] who concluded that the gradient Richardson number will produce less self-correlation than the stability parameter ζ.

In this section we are going to use the R_g as stability parameter to define the behaviour of the wind speed and potential temperature profiles thanks to the similarity functions $\Upsilon_m(\zeta, \zeta_{0m})$ and $\Upsilon_h(\zeta, \zeta_{0h})$. We don't have an analytical formula for $\Upsilon_m(R_g)$, therefore we had to extrapolate its behaviour. Both the gradient Richardson number R_g and the similarity functions Υ depend on ζ, therefore we can find a correlation between them. We calculated both this parameters varying ζ between $10^{-3} \div 10^2$. Therefore we wrote all data in a table having in each row the value for ζ, the values for R_g calculated with Eq. 1.49 for different authors ($H96$, $W70$ and $BH91$), and the value of $\Upsilon_m(\zeta, \zeta_{0m})$ and $\Upsilon_h(\zeta, \zeta_{0h})$ calculated with Eqs. 1.43,1.46 for the same authors. We then used the R_g and Υ columns to plot the required functions.

In Fig. 3.10 is shown the dependence of Υ_m on the gradient Richardson number R_g for three levels ($5.8m$, $13.5m$ and $32m$). The data plotted seem to follow the trend described by the new similarity functions, with a large scatter for high stability, especially at increasing height.

Fig. 3.11 is the same as the previous one, but we used the classification for the cases based on the wind speed defined in Section 2.7. The resulting data is well separated between those with $u > u_t(z)$, which better follow the overlayed functions, and those with $u < u_t(z)$, which are much more scattered.

The same behaviour can be seen in Figs. 3.12 and 3.13. In the first one is shown the dependence of Υ_h on the gradient Richardson number R_g for three levels ($5.55m$, $14.22m$ and $32m$), while in the second one the same data is plotted, but in this case they are separated by the cases defined by the wind speed.

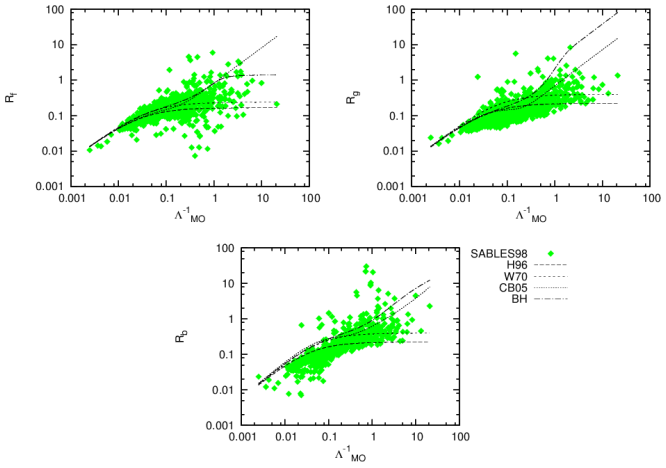

Figure 3.9: *Richardson numbers versus stability parameter* Λ_{MO}^{-1} *at z=5.8m. (a)* R_f*, (b)* R_g *and (c)* R_b*.*

We also note that for strong stability, Υ_m tends to level off while Υ_h has a positive trend. This evolution produces a ratio $\Upsilon_m/\Upsilon_h < 1$, which is equivalent to a greater turbulent transport of momentum compared to the transfer of heat. This result, not visible when $\zeta = z/\Lambda_{MO}$ is used as stability parameter, has been related to the presence of internal gravity waves (which can transport momentum but not much heat, unless they break), and associated intermittent processes (Finnigan et al. [1984], Coulter and Doran [2002], Mahrt [1989], Newsom and Banta [2003]).

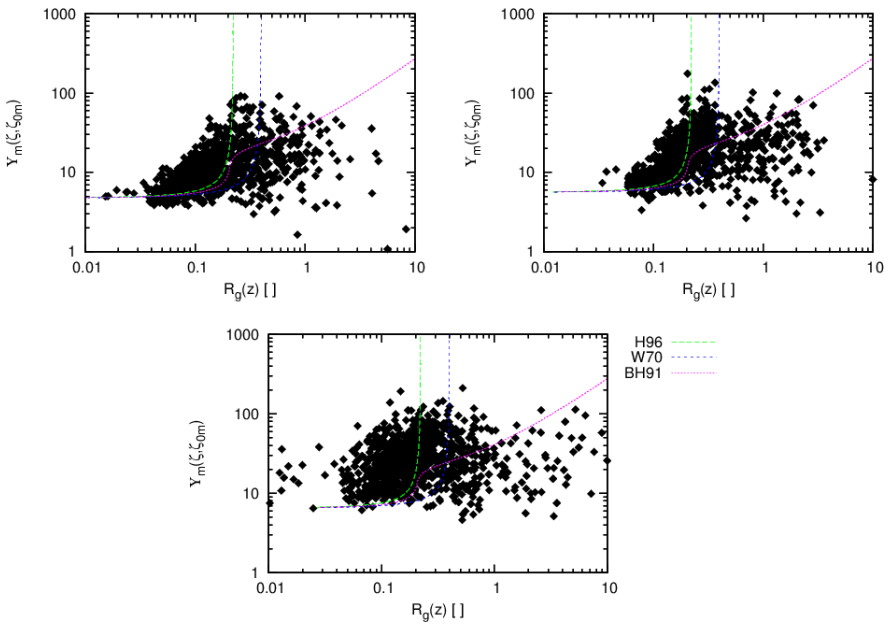

Figure 3.10: Υ_m *versus* $R_g(z)$ *for all the data in the dataset. Functions calculated from similarity functions of different authors are shown for comparison.*

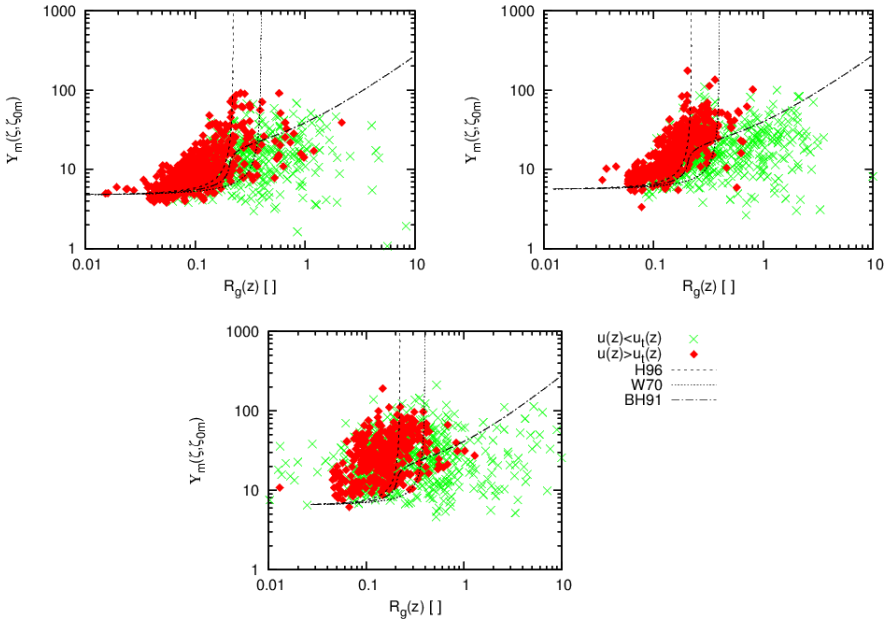

Figure 3.11: Υ_m *versus* $R_g(z)$ *for all the data in the dataset, divided by the wind speed as we defined in Chapter 2.7. Functions calculated from similarity functions of different authors are shown for comparison.*

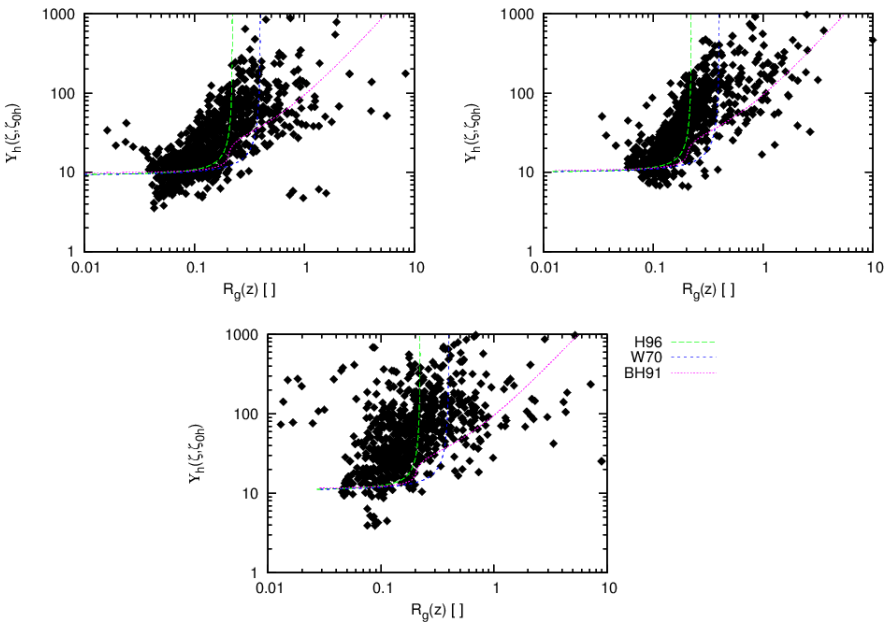

Figure 3.12: Υ_h *versus* $R_g(z)$ *for all the data in the dataset. Functions calculated from similarity functions of different authors are shown for comparison.*

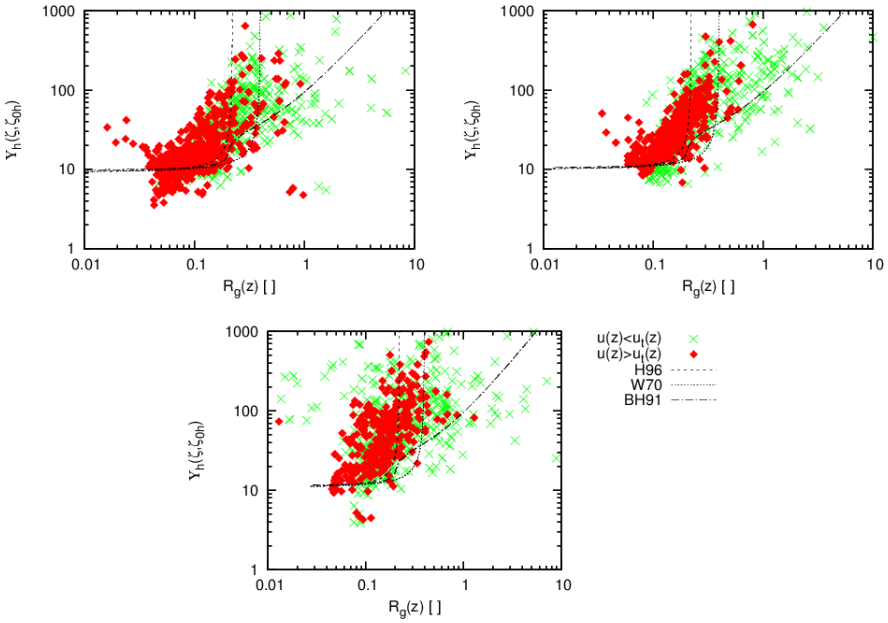

Figure 3.13: Υ_h *versus* $R_g(z)$ *for all the data in the dataset, divided by the wind speed as we defined in Chapter 2.7. Functions calculated from similarity functions of different authors are shown for comparison.*

Chapter 4

Conclusions

The first section of this work was an introductory overview of the structure of the atmosphere (Chapter 1.1), and in particular of its lower part, the atmospheric boundary layer (Chapter 1.2).

We described the turbulence (Chapter 1.4) and the equations that describe it (Chapter 1.5), noting that they form a non-closed system of equations, causing the impossibility to solve them analytically. For this reason, several closure methods have been developed over the years, and in particular we introduced Monin-Obukhov's similarity theory (Chapter 1.6).

The main objective of this study was to use the construct of this theory to analyze data collected during stable atmospheric conditions when the surface is cooler than the atmosphere, conditions achieved especially at night. The data was collected during the SABLES98 experiment, in Spain, during the month of September 1998 (Chapter 2.1).

We were interested in particular on the different structures that the stable boundary layer shows, mainly differentiating its behaviour based on the vertical fluxes of momentum and heat. We separated the SBL in two different categories, the traditional boundary layer (with decreasing fluxes with height) and the so called upside-down boundary layer (with increasing fluxes with height).

We analyzed portions of two different nights from the dataset, which represented the two contrasting structures of the stable boundary layer. We dedicated the following sections to the first analysis of the data for these two case studies, studying their behaviour in time and space (Chapters 2.3, 2.4).

We then developed an original criterion in order to distinguish and separate the influence of mesoscale phenomenons from turbulent behavior, using as parameters the wind speed and the gradient Richardson number (Chapter 2.7).

In the final chapter we tested different similarity functions developed by different authors. We compared them with the data from the experimental campaign and studied their behavior for the wind and for the temperature. We also used a method in order to eliminate some of the scatter of the data, removing from the equations the dependence on the surface roughness, parameter determined from the data, which can introduce errors.

We then determined how these similarity functions behave if expressed in terms of a different stability parameter, not ζ as defined in M-O similarity theory, but the gradient Richardson number R_g.

The primary result achieved in this study is the comparison between the two different classifications of the states of the stable boundary layer. The first one was based on the behavior of the vertical profiles of momentum and heat fluxes (defined as case 1 and 4). The second one, developed by the author, was based on the differentiation, through an analysis of the fluxes cospectra, of mesoscale phenomenons and the smaller scale turbulence.

The first difference that can be noticed is in regard of the height of the measurements. With the first classification, with increasing height, the cases tend to mix up and be undistinguishable from one another (e.g. Figs. 3.2, 3.5). Instead, with the second classification, the data tends to remain separated, and it is more clear the correlation with the similarity functions (e.g. Figs. 3.3, 3.6).

The similarity functions for wind and temperature, in both formulations

depending on the stability parameter ζ or R_g, seem to work well only for weak stability. In this case, the data follows with good agreement the trend of the similarity functions with relatively low scatter. In high stability conditions, instead, the scatter increases strongly, and in some cases the data presents a trend that is different from the one described by the similarity functions (e.g. Fig. 3.10).

Another difference between the considered classification of the cases is about the physics of the processes involved in them. In the first, we divided the cases based on the behavior of the fluxes, if they showed an increasing (case 4) or decreasing (case 1) trend with height. This distinction is based on the estimation of where the turbulence is produced, and therefore on how the transport of momentum and heat will shape the stable boundary layer. The second classification instead takes into account an original interpretation of the Multi-Resolution Flux decomposition, in order to find different parameters (in this study we decided for the gradient Richardson number R_g and the wind speed) which can separate the influence of mesoscale processes and the smaller scale turbulence.

Despite having different origins, there is a common point to both of these formulations. In fact, as it is possible to see in most of the figures in Chapter 3, the personal cases with weak stability ($R_g < 0.163$) and strong winds ($u(z) > u_t(z)$) tend to describe the same situations as those described with cases 1 (decreasing fluxes with height). This is in agreement with the previous statement that the similarity theories are better represented by the data in weak stability conditions.

A comparison of these two classification is visible in Figs. 4.1 and 4.2. We plotted the Υ_m and Υ_h similarity functions, and we showed only the data points which are shared between the two formulations. It is possible to see, comparing the first with Figs. 3.2, 3.3 and the second with Figs. 3.5, 3.6, that a good amount of the data points are shared between these two formulations, despite the very different physical processes that they describe.

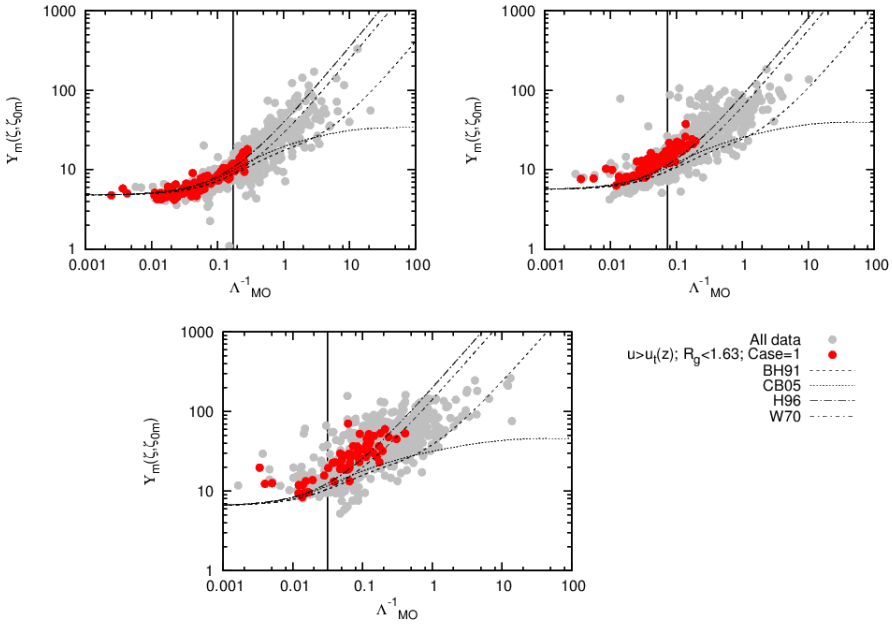

Figure 4.1: Υ_h *versus* Λ_{MO}^{-1} *for all the data in the dataset, showing the common data points between the different cases formulations.*

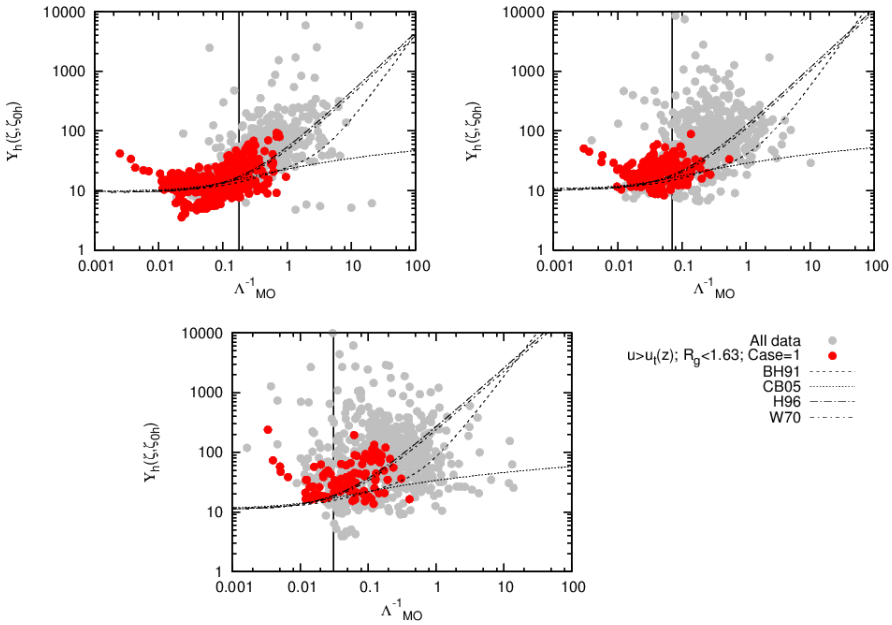

Figure 4.2: Υ_h *versus* Λ_{MO}^{-1} *for all the data in the dataset, showing the common data points between the different cases formulations.*

Acknowledgments

Thanks are due to Carlos Yagüe, Universidad Complutense de Madrid, who supplied the SABLES98 data used in this work.

I would like to thank most sincerefully Prof. Francesco Tampieri for his immense patience and dedication.

I would like to thank greatly my family, in particular my parents, Mauro and Candida, and my sister Giada, for their presence and support even when the times were not the happiest.

A special thanks to all of my friends, in particular to Paola, Barbara, Luca, Eleonora, Elena, because they are really awesome and supportive friends, and beacuse I spent some beautiful years in their company!

And finally I would like to thank immensely India, for her great help correcting all kinds of errors and because she is just amazing!

A big thanks to everyone else I didn't mention, because you are in my heart and mind, and because I wouldn't be here if it wasn't for every single one of you!

Bibliography

R. M. Banta. Stable-boundary-layer regimes from the perspective of the low-level jet. *Acta Geophysica*, 56(1):58–87, 2008.

R. M. Banta, R. K. Newsom, Julie K. Lundquist, Yelena L. Pichugina, R. L. Coulter, and Larry Mahrt. Nocturnal low-level jet characteristics over kansas during cases-99. *Boundary-Layer Meteorology*, 105:221–252, 2002.

R. M. Banta, Yelena L. Pichugina, and R. K. Newsom. Relationship between low-level jet properties and turbulence kinetic energy in the nocturnal stable boundary layer. *Journal of the atmospheric sciences*, 60:2549–2555, 2003.

R. M. Banta, Yelena L. Pichugina, and W. Alan Brewer. Turbulent velocity-variance profiles in the stable boundary layer generated by a nocturnal low-level jet. *J. Atmos. Sci.*, 63:2700–2719, 2006.

R. M. Banta, Larry Mahrt, Dean Vickers, Jielun Sun, B. B. Balsley, Yelena L. Pichugina, and Eric J. Williams. The very stable boundary layer on nights with weak low-level jets. *Journal of the Atmospheric Sciences*, 64:3068–3090, November 2007.

A.C.M Beljaars and A. A. M. Holtslag. Flux parameterization over land surfaces for atmospheric models. *J. Appl. Meteorol.*, 30:327–341, 1991.

S. J. Caughey, J. C. Wyngaard, and J. C. Kaimal. Turbulence in the evolving stable boundary layer. *J. Atmos. Sci.*, 36:1041–1052, 1979.

Y. Cheng and Wilfried Brutsaert. Fluxâprofile relationships for wind speed and temperature in the stable atmospheric boundary layer. *Boundary-Layer Meteorol.*, 114:519–538, 2005.

R. L. Coulter and J. C. Doran. Spatial and temporal occurrences of intermittent turbulence during cases-99. *Boundary-Layer Meteorology*, 105: 329–349, 2002.

J. Cuxart, C. Yague, G. Morales, E. Terradella, J. Orbe, J. Calvo, A. Fernandez, M. R. Soler, C. Infante, P. Buenestado, A. Espinalt, H. E. Joergensen, J. M. Rees, J. Vila, JosÃ© Manuel Redondo, I. R. Cantalapiedra, and L. Conangla. Stable atmospheric boundary-layer experiment in Spain (SABLES 98): a report. *Boundary-Layer Meteorol.*, 96:337–370, 2000.

Nelson L. Dias, Wilfried Brutsaert, and M. L. Wesely. Z-less stratification under stable conditions. *Boundary-Layer Meteorol.*, 75:175–187, 1995.

J.M. Edwards. Radiative processes in the stable boundary layer: Part ii. the development of the nocturnal boundary layer. *boundary-layer meteorology*, 131:127–146, 2009.

J. J. Finnigan, F. Einaudi, and D. Fua. The interaction between an internal gravity wave and turbulence in the stably stratified nocturnal boundary layer. *J. Atmos. Sci.*, 41:2409–2436, 1984.

J. R. Garratt. *The atmospheric boundary layer*. Cambridge University Press, 1992. 316 pp.

Andrey A. Grachev, Chris. W. Fairall, P. Ola G. Persson, E. L. Andreas, and Peter S. Guest. Stable boundary-layer scaling regimes: The sheba data. *Boundary-Layer Meteorology*, 116(2):201–235, August 2005.

Ulf Högström. Review of some basic characteristics of the atmospheric surface layer. *Boundary-Layer Meteorology*, 78:215–246, 1996.

J. F. Howell and L. Mahrt. Multiresolution flux decomposition. *Boundary-Layer Meteorology*, 83:117–137, 1997.

Cheryl L. Klipp and Larry Mahrt. Flux-gradient relationship, self-correlation and intermittency in the stable boundary layer. *Quarterly J. Royal Meteorol. Soc.*, 130:2087–2103, 2004.

A. K. Luhar, P. J. Hurley, and K. N. Rayner. Modelling near-surface low winds over land under stable conditions: sensitivity tests, flux-gradient relationships, and stability parameters. *Boundary-Layer Meteorol.*, 130 (2):249–274, 2009.

Larry Mahrt. Intermittency of atmospheric turbulence. *Journal of the Atmospheric Sciences*, 46(1):79–95, 1989.

Larry Mahrt. Stratified atmospheric boundary layers and breakdown of models. *Theoretical and Computational Fluid Dynamics*, 11:263–279, 1998.

Larry Mahrt. Stratified atmospheric boundary layers. *Boundary-Layer Meteorol.*, 90:375–396, 1999.

Larry Mahrt. The influence of nonstationarity on the turbulent fluxââgradient relationship for stable stratification. *Boundary-Layer Meteorology*, 125:245–264, 2007.

Larry Mahrt. The near-calm stable boundary layer. *Boundary-Layer Meteorology*, 140:343–360, 2011.

Larry Mahrt and Dean Vickers. Contrasting vertical structures of nocturnal boundary layers. *Boundary-Layer Meteorology*, 105:351–363, 2002.

Larry Mahrt, R. C. Heald, D. H. Lenschow, B. B. Stankov, and I. Troen. An observational study of the structure of the nocturnal boundary layer. *Boudary-Layer Meteorology*, 17:247–264, 1979.

A. S. Monin and A. M. Obukhov. Basic laws of turbulent mixing in the ground layer of the atmosphere. *Akad. Nauk SSSR*, 151:163–187, 1954.

R. K. Newsom and R. M. Banta. Shear-flow instability in the stable nocturnal boundary layer as observed by doppler lidar during cases-99. *Journal of the Atmospheric Sciences*, 60:16–33, 2003.

F. T. M. Nieuwstadt. Some aspects of the turbulent stable boundary layer. *Boundary-Layer Meteorology*, 30:31–55, 1984.

Markus Pahlow, M.B. Parlange, and Fernando Porte-Agel. On Monin-Obukhov similarity in the stable atmospheric boundary layer. *Boundary-Layer Meteorol.*, 99:225–248, 2001.

Z. Sorbjan and Andrey A. Grachev. An evaluation of the flux-gradient relationship in the stable boundary layer. *Boundary-Layer Meteorol.*, 135: 385–405, 2010.

R. Sozzi, T. Georgiadis, and M. Valentini. *Introduzione alla Turbolenza Atmosferica: Concetti, Stime, Misure*. Pitagora Editrice Bologna, 2002.

R. B. Stull. *An introduction to boundary layer meteorology*. Kluwer Academic Publishers, 1988.

Francesco Tampieri. Appunti sul corso di strato limite atmosferico e diffusione turbolenta, 2010.

H. Tennekes and J. L. Lumley. *A first course in turbulence*. MIT Press, Cambridge. 1972.

Fernanda Trombetti and Mauro Tagliazucca. Characteristic scales of atmospheric surface layer. Tech. Rep. FISBAT-TP-94/1, FISBAT, FISBAT CNR, via Gobetti 101, 40129 Bologna, Italy, 1994.

V. Voronovich and G. Kiely. On the gap in the spectra of surface-layer atmospheric turbulence. *Boundary-Layer Meteorology*, 122:67–83, 2007.

John M. Wallace and Peter V. Hobbs. *Atmospheric science: An introductory survey*. Academic Press, 2006.

E. K. Webb. Profile relationships: the log-linear range and extension to strong stability. *Quart. J. Roy. Meteorol. Soc.*, 96:67–90, 1970.

C. Yagüe, S. Viana, G. Maqueda, and José Maunel Redondo. Influence of stability on the flux-profile relationships for wind speed, ϕ_m, and temperature, ϕ_h, for the stable atmospheric boundary layer. *Nonlinear Proc. Geoph.*, 13:185–203, 2006.

S. S. Zilitinkevich and Alexander Baklanov. Calculation of the height of the stable boundary layer in practical applications. *Boundary layer meteorology*, 105:389–409, 2002.